Micromechanics-based prediction of the effective properties of piezoelectric composite having interfacial imperfections

Sangryun Lee[a], Jiyoung Jung[a], and Seunghwa Ryu[a,*]

Affiliations

[a]Department of Mechanical Engineering, Korea Advanced Institute of Science and Technology (KAIST), 291 Daehak-ro, Yuseong-gu, Daejeon 34141, Republic of Korea

[*]Corresponding author e-mail: ryush@kaist.ac.kr

Abstract

We derive an analytical expression to predict the effective properties of a particulate-reinforced piezoelectric composite with interfacial imperfections using a micromechanics-based mean–field approach. We correctly derive the analytical formula of the modified Eshelby tensor, the modified concentration tensor, and the effective property equations based on the modified Mori–Tanaka method in the presence of interfacial imperfections. Our results are validated against finite element analyses (FEA) for the entire range of interfacial damage levels, from a perfect to a completely disconnected and insulated interface. For the facile evaluation of the nontrivial tensorial equations, we adopt the Mandel notation to perform tensor operations with 9×9 symmetric matrix operations. We apply the method to predict the effective properties of a representative piezoelectric composite consisting of PVDF and SiC reinforcements.

Keywords

Piezoelectric composite, Eshelby tensor, Interfacial damage, Effective modulus

1. Introduction

Piezoelectricity refers to the electric charge accumulation in response to an applied mechanical loading, or, conversely, the mechanical strain generated from an applied electrical field (Cady, 1964). Such a characteristic has been extensively exploited in many important engineering applications such as high power generation (Lee et al., 2014; Yang et al., 2009), lightweight transducers (Guerin et al., 2019; Stamatellou and Kalfas, 2018), precision positioning stages of various microscopes (Li et al., 2019; Wang et al., 2019), vibration cancellation modules (Lin and Liu, 2006; Tan et al., 2019), and artificial skin of wearable devices (Chorsi et al., 2019; Yuan et al., 2019). Piezoelectricity occurs in a limited set of materials such as crystals with no inversion symmetry (Jella et al., 2019) and polymer materials with high dipolar moment (Ramadan et al., 2014). For example, one of the widely used piezoelectric polymers, polyvinylidene fluoride (PVDF), has five different crystalline phases: $\alpha, \beta, \gamma, \delta$, and ε. However, the α and ε phases have zero net dipole moment owing to their antiparallel chain structure, and thus, the β phase, which has the highest net dipole moment, has been primarily used (Ramadan et al., 2014). Owing to the limited numbers of piezoelectric materials, it often becomes difficult to obtain a piezoelectric material that simultaneously satisfies the multiple requirements of a given application. For example, the pure PVDF polymer has a small elastic stiffness (~3 GPa), which limits its applicability (Pei and Zeng, 2011).

Hence, various piezoelectric composites have been fabricated such as the lead zirconate titanate (PZT)–polymer composite (Almusallam et al., 2015; Venkatragavaraj et al., 2001) for an enhanced dielectric and hydrostatic piezoelectric coefficient and polyvinylidene difluoridein (PVDF)–SiC composite (Zhang et al., 2015; Zhou et al., 2015) for improved dielectric permittivity and elastic stiffness. Further, physical reinforcements as well as voids

are known to improve some properties, i.e., the hydrostatic piezoelectric figure of merit increases with porosity (Zhang et al., 2017). Therefore, for the efficient design of a piezoelectric composite, it is essential to predict the effective properties of the reinforced piezoelectric composites in terms of its size, shape, and volume fraction of reinforcements.

The Mori–Tanaka method, a micromechanics-based mean–field homogenization approaches, has been used to predict various effective physical properties of a reinforced composite, such as the elastic constant (Benveniste, 1987; Lee et al., 2019a; Lee and Ryu, 2018), thermal conductivity (Lee et al., 2018; Quang et al., 2011), dielectric constant (Giordano and Palla, 2008), and thermoelectric (Jung et al., 2018) and piezoelectric properties (Odegard, 2004; Wang et al., 2014a; Wang et al., 2014c). The Mori–Tanaka method was originally developed to predict the effective elastic properties of particulate-reinforced composite by using the Eshelby tensor for a composite involving multiple inhomogeneities with the mean–field approximation (Benveniste, 1987). The method has also been extended to predict other physical properties based on the mathematical analogy with steady-state governing equations (Ryu et al., 2019). Dunn and Taya were the first to adapt the Mori–Tanaka approach to model the piezoelectric composite by assuming a perfect interface between the reinforcement and the matrix (Dunn and Taya, 1993a, c). However, a realistic piezoelectric composite interface may exhibit imperfections such as the displacement jump (Zhao et al., 2012) or the electric compliance (Kim et al., 2011). Such interfacial imperfections can significantly affect the effective piezoelectric properties of a nanocomposite with nanoscale reinforcements that has a significantly higher interfacial area compared to a composite involving macroscale reinforcements with an identical volume fraction.

To consider these interfacial imperfections, previous studies attempted to extend the

Mori–Tanaka method by deriving the modified Eshelby tensor and the modified concentration tensor in the presence of interfacial imperfections (Wang et al., 2014a; Wang et al., 2014b; Wang et al., 2014c). However, as shown in the later part of this article, we find that the analytical expressions do not match with the FEA because the modified Eshelby tensor was derived by violating the Fubini–Tonelli theorem (Folland, 2013), and the modified concentration tensor was derived without considering the additional displacement jump and the discontinuity in electric potential.

Here, we correctly derive analytical expressions of the modified Eshelby tensor and the modified concentration tensor of a piezoelectric material that are applicable to a material with arbitrary symmetry, and use them to predict the effective properties of piezoelectric composites. For the facile evaluation of the nontrivial tensor equations, we adopt the Mandel notation (Lee et al., 2019b), rather than the Voigt notation, to perform tensor operations with 9×9 symmetric matrix operations. The analytical results are validated against the FEA results. We applied our results to predict the effective elastic modulus, piezoelectric constant, dielectric constant, and figure of merit map of the PVDF-SiC composite.

The rest of this paper is organized as follows. First, in Section 2, we define the piezoelectric modulus and derive the modified Eshelby tensor for the piezoelectric composite in the presence of interfacial imperfections. We also show that the Mori–Tanaka method is not applicable for non-spherical inclusions, comprising elliptical inclusions with an aspect ratio other than 1, because of the non-uniform interior strain and electric field. In Section 3, we derive the modified concentration tensor in terms of the piezoelectric moduli of matrix and reinforcement, the degree of interfacial imperfection, and the Eshelby tensor. In Section 4, •e derive the expression for the effective piezoelectric modulus and obtain the effective dielectric constant, effective elastic modulus, effective piezoelectric coefficient, and effective

figure of merit for a representative piezoelectric composite consisting of PVDF and SiC. We present the concluding remarks in Section 5.

2. Modified Eshelby tensor for piezoelectric properties

2.1 Constitutive equation and governing equation for piezoelectric material

We choose the elastic strain (ε_{ij}) and electric field (E_i) as two independent input variables and relate them with the output variables, mechanical stress (σ_{ij}) and electric displacement(D_i). The constitutive and governing equations of the piezoelectric material are expressed as Eq. (1) and Eq. (2), respectively,

$$\begin{aligned} \sigma_{ij} &= C_{ijmn}\varepsilon_{mn} + e_{nij}(-E_n) \\ D_i &= e_{imn}\varepsilon_{mn} - \kappa_{in}(-E_n) \end{aligned} \tag{1}$$

$$\begin{aligned} \sigma_{ij,i} &= 0 \\ D_{i,i} &= 0 \end{aligned} \tag{2}$$

where C_{ijmn}, e_{nij}, and κ_{in} are the elastic constant, piezoelectric constant, and dielectric constant, respectively. The repeated index is a dummy index, which implies the summation over all values, 1 to 3. Eq. (1) can be shortened by adopting the notation suggested by Barnett and Lothe (Barnett and Lothe, 1975).

$$\Sigma_{iJ} = L_{iJMn}Z_{Mn} \tag{3}$$

By adapting the notation, one can construct a constitutive equation having a similar form with linear elastostatics (Hooke's law) or heat conduction (Fourier's law). The repeated capital subscripts are summed over 1–4 and L_{iJMn} is a piezoelectric moduli tensor which can be constructed by

$$L_{iJMn} = \begin{cases} C_{ijmn} & J, M = 1,2,3 \\ e_{nij} & J = 1,2,3, M = 4 \\ e_{imn} & J = 4, M = 1,2,3 \\ -\kappa_{in} & J, M = 4 \end{cases} \tag{4}$$

Z_{Mn} is the extended strain obtained from the extended displacement U_M, which is written as

$$Z_{Mn} = \frac{dU_M}{\partial x_n}, \quad U_M = \begin{cases} u_M & M = 1,2,3 \\ \phi & M = 4 \end{cases} \tag{5}$$

where u_M and ϕ are the displacement and potential field, respectively. Similarly, the extended stress Σ_{iJ} is expressed as

$$\Sigma_{iJ} = \begin{cases} \sigma_{iJ} & J = 1,2,3 \\ D_i & J = 4 \end{cases}. \tag{6}$$

Based on the notation, one can express the governing equation for the Green's function of a piezoelectric material as

$$L_{iJKl} \frac{\partial^2 G_{KM}(\boldsymbol{x} - \boldsymbol{y})}{\partial x_i \partial x_l} + \delta_{JM} \delta(\boldsymbol{x} - \boldsymbol{y}) = 0. \tag{7}$$

which is mathematically analogous with the steady-state governing equations of other physical phenomena such as elastostatics (Lee et al., 2019b), heat conduction (Lee et al., 2018; Quang et al., 2011), and thermoelectricity (Jung et al., 2018). Following previous studies (Dunn and Taya, 1993a), the Green's function of a piezoelectric material is expressed as

$$G_{KM}(\boldsymbol{x} - \boldsymbol{y}) = \frac{1}{8\pi |\boldsymbol{x} - \boldsymbol{y}|} \int_{|z|=1} K_{KM}^{-1} \delta \left(\boldsymbol{z} \cdot \left(\frac{\boldsymbol{x} - \boldsymbol{y}}{|\boldsymbol{x} - \boldsymbol{y}|} \right) \right) dS(\boldsymbol{z}) \tag{8}$$

where K_{KM}^{-1} is the inverse of

$$K_{KM} = z_i z_n L_{iKMn} \tag{9}$$

For elasticity and the heat conduction problem, the Green's functions have been derived in closed form even for an anisotropic material (Lee et al., 2018; Mura, 1982). However, it is

difficult to derive the closed form of the Green's function of a piezoelectric material owing to the mathematical complexity arising from the coupling (piezoelectric) constant (Huang and Yu, 1994).

2.2 Eshelby's single inclusion problem in the absence of interfacial imperfection

The single inclusion problem of a piezoelectric material can be explained by the following four steps (Fig. 1). When the inclusion with a nonzero extended eigenstrain(Z^*_{Ab}) is released after its insertion into the matrix having a same size hole, the inclusion deforms less than the (extended) eigenstrain owing to the interaction with the matrix. Based on the mathematical analogy between elasticity and piezoelectricity, one can realize that the constrained extended strain field within the inclusion is uniform when the shape of the inclusion is ellipsoid. Therefore, the constrained (extended) displacement and strain field are expressed as

$$U_M = \int_{\partial\Omega} G_{MJ}(\boldsymbol{x}-\boldsymbol{y})\Sigma^*_{qJ} n_q d\boldsymbol{y} = \int_{\partial\Omega} G_{MJ}(\boldsymbol{x}-\boldsymbol{y}) L_{qJAb} Z^*_{Ab} n_q d\boldsymbol{y}$$

$$Z_{Mn} = S_{MnAb} Z^*_{Ab}, \qquad S_{MnAb} = \int_{\Omega} P_{MnJq} d\boldsymbol{y}\, L_{qJAb} \tag{10}$$

$$\text{where} \quad P_{MnJq} = \begin{cases} \dfrac{1}{2}\left(\dfrac{\partial^2 G_{MJ}}{\partial x_n \partial y_q} + \dfrac{\partial^2 G_{nJ}}{\partial x_M \partial y_q}\right) & M = 1,2,3 \\ \dfrac{\partial^2 G_{MJ}}{\partial x_n \partial y_q} & M = 4 \end{cases}$$

where $\partial\Omega$ is the surface of the inclusion and S_{MnAb} is Eshelby tensor of the piezoelectric material. As suggested by Dunn and Taya (Dunn and Taya, 1993a, c), the Eshelby tensor of a piezoelectric ellipsoid having semi-axes as $a_1, a_2,$ and a_3 can be expressed in alternative form as

$$S_{MnAb} = \begin{cases} \frac{1}{8\pi} L_{iJAb} \int_{-1}^{1} \int_{0}^{2\pi} \left[\Phi_{MJin}(\boldsymbol{z}) + \Phi_{nJiM}(\boldsymbol{z}) \right] d\theta d\xi_3 & M = 1,2,3 \\ \frac{1}{4\pi} L_{iJAb} \int_{-1}^{1} \int_{0}^{2\pi} \left[\Phi_{MJin}(\boldsymbol{z}) \right] d\theta d\xi_3 & M = 4 \end{cases} \tag{11}$$

where $\Phi_{MJin}(\boldsymbol{z}) = z_i z_n K_{MJ}^{-1}(\boldsymbol{z})$ and $z_1 = \sqrt{1-\xi_3^2}\cos\theta/a_1$, $z_2 = \sqrt{1-\xi_3^2}\sin\theta/a_2$, $z_3 = \xi_3/a_3$. As for the Green's function, it is also difficult to obtain the closed-form expression because of the piezoelectric coupling constants (Huang and Yu, 1994; Mikata, 2001).

2.3 Imperfect interface modelled by linear spring model

Eq. (10) assumes perfect bonding at the interface without displacement or electric potential discontinuity. We adopt the linear spring model to account for the interfacial damage for mechanical response for mathematical simplicity, and consider a dielectric layer at the interface to model the interfacial damage for electrical response (Fig. 2). For a piezoelectric material, the constitutive equation at the damaged interface is expressed as

$$\begin{aligned} \Delta T_J &= \Delta \Sigma_{iJ} n_i = \left(\Sigma_{iJ}(\partial\Omega^+) - \Sigma_{iJ}(\partial\Omega^-) \right) n_i = 0 \\ \Delta U_J &= U_J(\partial\Omega^+) - U_J(\partial\Omega^-) = \Lambda_{JM} \Sigma_{iM} n_i \end{aligned} \tag{12}$$

where $\partial\Omega^+$ and $\partial\Omega^-$ denote the interface surface on the matrix and inclusion side, respectively (Fig. 2). Λ_{JM} represents the extended interface spring compliance expressed as

$$\Lambda_{JM} = \begin{cases} \alpha\delta_{JM} + (\beta - \alpha) n_J n_M & J = 1,2,3, M = 1,2,3 \\ -\gamma & J = M = 4 \\ 0 & \text{others} \end{cases} . \tag{13}$$

α, β represent the tangential and normal direction spring compliance, respectively, and γ is the electric compliance coefficient. α, β are equivalent to the small-deformation-regime compliances of the cohesive zone models that are widely adapted in various FEA studies (Bouhala et al., 2013; Fan and Tadmor, 2019; Springer et al., 2019). Thus, α, β are always

positive. γ represents the effect of a dielectric layer at the interface and is mathematically analogous with Kapitza's resistance in a heat conduction problem (Lee et al., 2018; Quang et al., 2011). As expressed in Eq. (12), large interfacial damage results in large displacement (potential) jump across the interface and zero interfacial damage implies perfect bonding.

The extended strain field within the single inclusion having the interfacial imperfection can be expressed as follows:

$$\begin{aligned} Z_{Mn}(\boldsymbol{x}) &= S_{MnRs}Z^*_{Rs} + \int_{\partial\Omega} \Delta U_J L_{iJKl} P_{MnKl} n_i d\boldsymbol{y} \\ &= S_{MnRs}Z^*_{Rs} + \int_{\partial\Omega} \Lambda_{JP}\Sigma_{qP} n_q L_{iJKl} P_{MnKl} n_i d\boldsymbol{y} \\ &= S_{MnRs}Z^*_{Rs} + \int_{\partial\Omega} \Lambda_{JP} L_{qPRs}(Z_{Rs} - Z^*_{Rs}) n_q L_{iJKl} P_{MnKl} n_i d\boldsymbol{y} \end{aligned} \tag{14}$$

In general, the constrained strain field within an ellipsoidal inclusion is non-uniform when the interfacial compliances are finite (Appendix A). Thus, it is difficult to express the strain field in the closed form because Eq. (14) is an implicit equation involving $\boldsymbol{Z}$ in both the left and right sides. Previous studies (Wang et al., 2014a; Wang et al., 2014b; Wang et al., 2014c) have calculated the volume averaged modified Eshelby tensor to consider a non-uniform field, as expressed in Eq. (15).

$$\begin{aligned} \bar{Z}_{Mn} &= \frac{1}{\Omega}\int_{\Omega} Z_{Mn}(\boldsymbol{x})\, d\boldsymbol{x} \\ &= S_{MnRs}Z^*_{Rs} + \frac{1}{\Omega}\int_{\Omega} \left[\int_{\partial\Omega} \Lambda_{JP} L_{qPRs}(Z_{Rs} - Z^*_{Rs}) n_q L_{iJKl} P_{MnKl} n_i d\boldsymbol{y}\right] d\boldsymbol{x} \end{aligned} \tag{15}$$

The volume averaged modified Eshelby tensor was simplified after changing the order of surface integral and volume integral. A similar simplification has also been used for elasticity (Barai and Weng, 2011; Qu, 1993; Yanase and Ju, 2012) and heat conduction problems

(Bonfoh et al., 2017). However, according to the Fubini–Tonelli theorem, it is not legitimate to change the order of two integrals because the Green's function contains a singularity within the integral domain (Folland, 2013). We present a representative example of the violation of the Fubini–Tonelli theorem by considering a simple 2D integral problem in Appendix B.

In this study, we derive the modified Eshelby tensor without any approximation. In previous papers on elasticity (Lee et al., 2019b; Zhong and Meguid, 1997), it has been proved that the strain field within the spherical inclusion is uniform when $\alpha = \beta$, and for the heat conduction problem it is known that under finite Kapitza's resistance the intensity field (gradient of temperature) is uniform when the shape of the inclusion is spherical (Lee et al., 2018; Quang et al., 2011). Therefore, using a mathematical analogy (Ryu et al., 2019), we can deduce that the extended strain field within the piezoelectric inclusion is also uniform when the shape of the inclusion is spherical and $\alpha = \beta$ (Appendix A).

For the spherical inclusion problem with interfacial compliance $\alpha = \beta$, Eq. (14) is simplified as follows:

$$\begin{aligned} Z_{Mn}(\boldsymbol{x}) &= S_{MnRs} Z^*_{Rs} + \Lambda_{JP} L_{qPRs} L_{iJKl} \int_{\partial\Omega} P_{MnKl} n_i n_q d\boldsymbol{y} \, (Z_{Rs} - Z^*_{Rs}) \\ &= S_{MnRs} Z^*_{Rs} - \Gamma_{MnRs} (Z_{Rs} - Z^*_{Rs}) \end{aligned} \tag{16}$$

where

$$\Gamma_{MnRs} \equiv - \int_{\partial\Omega} \Lambda_{JP} L_{qPRs} L_{iJKl} P_{MnKl} n_i n_q d\boldsymbol{y} \tag{17}$$

By using $n_q = y_q / a$ and applying the divergence theorem on Γ_{MnRs}, Eq. (17) is further simplified as

$$\Gamma_{MnRs} = -\int_{\partial\Omega} \Lambda_{JP} L_{qPRs} L_{iJKl} P_{MnKl} n_i(\boldsymbol{y}) n_q(\boldsymbol{y}) d\boldsymbol{y}$$

$$= -\Lambda_{JP} L_{qPRs} \left[\int_{\Omega} L_{iJKl} P_{MnKl} \frac{\delta_{iq}}{a} d\boldsymbol{y} + \int_{\Omega} E_{iJKl} \frac{\partial P_{MnKl}}{\partial y_i} \frac{y_q}{a} d\boldsymbol{y} \right] \tag{18}$$

$$= -\Lambda_{JP} L_{qPRs} \frac{1}{a} \left[\int_{\Omega} L_{lKJq} P_{MnKl} d\boldsymbol{y} + \int_{\Omega} E_{iJKl} \frac{\partial P_{MnKl}}{\partial y_i} y_q d\boldsymbol{y} \right]$$

where a is the radius of the inclusion. Noting that the first integral term on the right hand side is the definition of the Eshelby tensor shown in Eq. (10), one can write the Eq. (18) as follows:

$$\begin{aligned} \Gamma_{MnRs} &= -\Lambda_{JP} E_{qPRs} \frac{1}{a} \left[\int_{\Omega} E_{lKJq} P_{MnKl} d\boldsymbol{y} + \int_{\Omega} E_{iJKl} \frac{\partial P_{MnKl}}{\partial y_i} y_q d\boldsymbol{y} \right] \\ &= -\Lambda_{JP} E_{qPRs} \frac{1}{a} \left[S_{MnJq} + \int_{\Omega} E_{iJKl} \frac{\partial P_{MnKl}}{\partial y_i} y_q d\boldsymbol{y} \right] \end{aligned} \tag{19}$$

To further simplify Eq. (19), we consider the following equation which is obtained by multiplying y_q after differentiating Eq. (7) with respect to y_n.

$$L_{iJKl} \frac{\partial^3 G_{KM}(\boldsymbol{x}-\boldsymbol{y})}{\partial y_n \partial y_i \partial y_l} y_q + \frac{\partial}{\partial y_n} \left(\delta_{JM} \delta(\boldsymbol{x}-\boldsymbol{y}) \right) y_q = 0 \tag{20}$$

Applying the divergence theorem after integrating Eq. (20) for the inclusion volume, we obtain

$$\begin{aligned} \int_{\Omega} L_{iJKl} \frac{\partial^3 G_{KM}(\boldsymbol{x}-\boldsymbol{y})}{\partial y_n \partial y_i \partial y_l} y_q d\boldsymbol{y} &= -\int_{\Omega} \frac{\partial}{\partial y_n} \left(\delta_{JM} \delta(\boldsymbol{x}-\boldsymbol{y}) \right) y_q d\boldsymbol{y} \\ &= -\int_{\Omega} \left(\delta_{JM} \delta(\boldsymbol{x}-\boldsymbol{y}) \right) \frac{\partial y_q}{\partial y_n} d\boldsymbol{y} \\ &= \delta_{JM} \delta_{nq}. \end{aligned} \tag{21}$$

Therefore,

$$\int_{\Omega} L_{iJKl}\frac{\partial P_{MnKl}}{\partial y_i}y_q d\boldsymbol{y} = \begin{cases} -\frac{1}{2}\left(\delta_{jm}\delta_{nq}+\delta_{jn}\delta_{mg}\right) & M=1,2,3 \\ -\delta_{JM}\delta_{nq} & M=4 \end{cases} \tag{22}$$

After putting Eq. (22) into Eq. (19), we can express Γ_{MnRs} as

$$\Gamma_{MnRs} = \Lambda_{JP}L_{qPRs}\frac{1}{a}\left(I_{MnJq}-S_{MnJq}\right).$$

$$\text{where} \qquad I_{MnJq} = \begin{cases} \frac{1}{2}\left(\delta_{jm}\delta_{nq}+\delta_{jn}\delta_{mg}\right) & M=1,2,3 \\ \delta_{JM}\delta_{nq} & M=4 \end{cases} \tag{23}$$

When $\alpha=\beta$, the extended interfacial compliance Λ_{JP} is simplified as Eq. (24), and thus, Eq. (23) can be rewritten as Eq. (25)

$$\Lambda_{JP} = \begin{cases} \alpha\delta_{jp} & J=P=1,2,3 \\ -\gamma\delta_{JP} & J=P=4 \end{cases} \tag{24}$$

$$\Gamma_{MnRs} = \sum_{J=1}^{4}\omega^J\delta_{JP}L_{qPRs}\frac{1}{a}\left(I_{MnJq}-S_{MnJq}\right)$$

$$= \sum_{J=1}^{4}\frac{\omega^J}{a}\left(I_{MnJq}-S_{MnJq}\right)L_{qJRs} \tag{25}$$

$$\text{where} \qquad \omega^J = \begin{cases} \alpha & J=1,2,3 \\ -\gamma & J=4 \end{cases}$$

Eq. (25) is mathematically analogous with $\boldsymbol{\Gamma}$ in other physical phenomena such as elasticity (Lee et al., 2019a; Lee et al., 2019b; Othmani et al., 2011), heat conduction (Lee et al., 2018; Quang et al., 2011), and thermoelectricity (Jung et al., 2018). Combining Eq. (16) and (25), we can predict the modified Eshelby tensor as

$$\boldsymbol{Z} = \boldsymbol{S}^M : \boldsymbol{Z}^*$$

$$\boldsymbol{S}^M = (\boldsymbol{I}+\boldsymbol{\Gamma})^{-1} : (\boldsymbol{S}+\boldsymbol{\Gamma}), \tag{26}$$

where : denotes a double contraction which implies $\boldsymbol{S}^M : \boldsymbol{Z}^* = S^M_{MnRs}Z^*_{RS}$.

2.4 Mandel notation

To evaluate Eq. (26), the inverse and double contraction of $4 \times 3 \times 4 \times 3$ or $3 \times 4 \times 4 \times 3$ tensors is required. Most papers concerning the micromechanics study of a piezoelectric material have adopted the Voigt notation to carry out the tensor operations (Martinez-Ayuso et al., 2017; Odegard, 2004; Wang et al., 2014c). Here, we adopt the Mandel notation because it is impossible to correctly calculate the modified Eshelby tensor with the Voigt notation. When the Voigt notation is adopted, the extended stress and strain vector expressed in Eq. (27) and the coefficient multiplied on components in the transformed 9×9 matrix depend on the type of the tensor.

$$\langle \boldsymbol{\Sigma} \rangle^{\mathrm{Voigt}} = \begin{bmatrix} \sigma_{11} \\ \sigma_{22} \\ \sigma_{33} \\ \sigma_{23} \\ \sigma_{31} \\ \sigma_{12} \\ D_1 \\ D_2 \\ D_3 \end{bmatrix}, \qquad \langle \boldsymbol{Z} \rangle^{\mathrm{Voigt}} = \begin{bmatrix} \varepsilon_{11} \\ \varepsilon_{22} \\ \varepsilon_{33} \\ 2\varepsilon_{23} \\ 2\varepsilon_{31} \\ 2\varepsilon_{12} \\ -E_1 \\ -E_2 \\ -E_3 \end{bmatrix} \tag{27}$$

For example, the transformed piezoelectric tensor $\langle \boldsymbol{L} \rangle^{\mathrm{Voigt}}$, Eshelby tensor $\langle \boldsymbol{S} \rangle^{\mathrm{Voigt}}$, and inverse of piezoelectric tensor $\langle \boldsymbol{M} \rangle^{\mathrm{Voigt}} = \langle \boldsymbol{L^{-1}} \rangle^{\mathrm{Voigt}}$ are expressed as

$$\langle \boldsymbol{L} \rangle^{\mathrm{Voigt}} = \begin{bmatrix} L_{1111} & L_{1122} & L_{1133} & L_{1123} & L_{1131} & L_{1112} & L_{1141} & L_{1142} & L_{1143} \\ L_{2211} & L_{2222} & L_{2233} & L_{2223} & L_{2231} & L_{2212} & L_{2241} & L_{2242} & L_{2243} \\ L_{3311} & L_{3322} & L_{3333} & L_{3323} & L_{3331} & L_{3312} & L_{3341} & L_{3342} & L_{3343} \\ L_{2311} & L_{2322} & L_{2333} & L_{2323} & L_{2331} & L_{2312} & L_{2341} & L_{2342} & L_{2343} \\ L_{3111} & L_{3122} & L_{3133} & L_{3123} & L_{3131} & L_{3112} & L_{3141} & L_{3142} & L_{3143} \\ L_{1211} & L_{1222} & L_{1233} & L_{1223} & L_{1231} & L_{1212} & L_{1241} & L_{1242} & L_{1243} \\ L_{1411} & L_{1422} & L_{1433} & L_{1423} & L_{1431} & L_{1412} & L_{1441} & L_{1442} & L_{1443} \\ L_{2411} & L_{2422} & L_{2433} & L_{2423} & L_{2431} & L_{2412} & L_{2441} & L_{2442} & L_{2443} \\ L_{3411} & L_{3422} & L_{3433} & L_{3423} & L_{3431} & L_{3412} & L_{3441} & L_{3442} & L_{3443} \end{bmatrix} \tag{28}$$

$$\langle \boldsymbol{S} \rangle^{\text{Voigt}} = \begin{bmatrix} S_{1111} & S_{1122} & S_{1133} & S_{1123} & S_{1131} & S_{1112} & S_{1141} & S_{1142} & S_{1143} \\ S_{2211} & S_{2222} & S_{2233} & S_{2223} & S_{2231} & S_{2212} & S_{2241} & S_{2242} & S_{2243} \\ S_{3311} & S_{3322} & S_{3333} & S_{3323} & S_{3331} & S_{3312} & S_{3341} & S_{3342} & S_{3343} \\ 2S_{2311} & 2S_{2322} & 2S_{2333} & 2S_{2323} & 2S_{2331} & 2S_{2312} & 2S_{2341} & 2S_{2342} & 2S_{2343} \\ 2S_{3111} & 2S_{3122} & 2S_{3133} & 2S_{3123} & 2S_{3131} & 2S_{3112} & 2S_{3141} & 2S_{3142} & 2S_{3143} \\ 2S_{1211} & 2S_{1222} & 2S_{1233} & 2S_{1223} & 2S_{1231} & 2S_{1212} & 2S_{1241} & 2S_{1242} & 2S_{1243} \\ S_{4111} & S_{4122} & S_{4133} & S_{4123} & S_{4131} & S_{4112} & S_{4141} & S_{4142} & S_{4143} \\ S_{4211} & S_{4222} & S_{4233} & S_{4223} & S_{4231} & S_{4212} & S_{4241} & S_{4242} & S_{4243} \\ S_{4311} & S_{4322} & S_{4333} & S_{4323} & S_{4331} & S_{4312} & S_{4341} & S_{4342} & S_{4343} \end{bmatrix}$$

$$\langle \boldsymbol{M} \rangle^{\text{Voigt}} = \begin{bmatrix} M_{1111} & M_{1122} & M_{1133} & 2M_{1123} & 2M_{1131} & 2M_{1112} & M_{1141} & M_{1142} & M_{1143} \\ M_{2211} & M_{2222} & M_{2233} & 2M_{2223} & 2M_{2231} & 2M_{2212} & M_{2241} & M_{2242} & M_{2243} \\ M_{3311} & M_{3322} & M_{3333} & 2M_{3323} & 2M_{3331} & 2M_{3312} & M_{3341} & M_{3342} & M_{3343} \\ 2M_{2311} & 2M_{2322} & 2M_{2333} & 4M_{2323} & 4M_{2331} & 4M_{2312} & 2M_{2341} & 2M_{2342} & 2M_{2343} \\ 2M_{3111} & 2M_{3122} & 2M_{3133} & 4M_{3123} & 4M_{3131} & 4M_{3112} & 2M_{3141} & 2M_{3142} & 2M_{3143} \\ 2M_{1211} & 2M_{1222} & 2M_{1233} & 4M_{1223} & 4M_{1231} & 4M_{1212} & 2M_{1241} & 2M_{1242} & 2M_{1243} \\ M_{1411} & M_{1422} & M_{1433} & 2M_{1423} & 2M_{1431} & 2M_{1412} & M_{1441} & M_{1442} & M_{1443} \\ M_{2411} & M_{2422} & M_{2433} & 2M_{2423} & 2M_{2431} & 2M_{2412} & M_{2441} & M_{2442} & M_{2443} \\ M_{3411} & M_{3422} & M_{3433} & 2M_{3423} & 2M_{3431} & 2M_{3412} & M_{3441} & M_{3442} & M_{3443} \end{bmatrix}$$

If the Mandel notation is used, the extended stress and strain vector is written as

$$\langle \boldsymbol{\Sigma} \rangle^{\text{Mandel}} = \begin{bmatrix} \sigma_{11} \\ \sigma_{22} \\ \sigma_{33} \\ \sqrt{2}\sigma_{23} \\ \sqrt{2}\sigma_{31} \\ \sqrt{2}\sigma_{12} \\ D_1 \\ D_2 \\ D_3 \end{bmatrix}, \qquad \langle \boldsymbol{Z} \rangle^{\text{Mandel}} = \begin{bmatrix} \varepsilon_{11} \\ \varepsilon_{22} \\ \varepsilon_{33} \\ \sqrt{2}\varepsilon_{23} \\ \sqrt{2}\varepsilon_{31} \\ \sqrt{2}\varepsilon_{12} \\ -E_1 \\ -E_2 \\ -E_3 \end{bmatrix} \tag{29}$$

and $\langle \boldsymbol{L} \rangle^{\text{Mandel}}, \langle \boldsymbol{S} \rangle^{\text{Mandel}}, \langle \boldsymbol{M} \rangle^{\text{Mandel}}$ is expressed as

$$\langle \boldsymbol{L} \rangle^{\text{Mandel}} = \begin{bmatrix} L_{1111} & L_{1122} & L_{1133} & \sqrt{2}L_{1123} & \sqrt{2}L_{1131} & \sqrt{2}L_{1112} & L_{1141} & L_{1142} & L_{1143} \\ L_{2211} & L_{2222} & L_{2233} & \sqrt{2}L_{2223} & \sqrt{2}L_{2231} & \sqrt{2}L_{2212} & L_{2241} & L_{2242} & L_{2243} \\ L_{3311} & L_{3322} & L_{3333} & \sqrt{2}L_{3323} & \sqrt{2}L_{3331} & \sqrt{2}L_{3312} & L_{3341} & L_{3342} & L_{3343} \\ \sqrt{2}L_{2311} & \sqrt{2}L_{2322} & \sqrt{2}L_{2333} & 2L_{2323} & 2L_{2331} & 2L_{2312} & \sqrt{2}L_{2341} & \sqrt{2}L_{2342} & \sqrt{2}L_{2343} \\ \sqrt{2}L_{3111} & \sqrt{2}L_{3122} & \sqrt{2}L_{3133} & 2L_{3123} & 2L_{3131} & 2L_{3112} & \sqrt{2}L_{3141} & \sqrt{2}L_{3142} & \sqrt{2}L_{3143} \\ \sqrt{2}L_{1211} & \sqrt{2}L_{1222} & \sqrt{2}L_{1233} & 2L_{1223} & 2L_{1231} & 2L_{1212} & \sqrt{2}L_{1241} & \sqrt{2}L_{1242} & \sqrt{2}L_{1243} \\ L_{1411} & L_{1422} & L_{1433} & \sqrt{2}L_{1423} & \sqrt{2}L_{1431} & \sqrt{2}L_{1412} & L_{1441} & L_{1442} & L_{1443} \\ L_{2411} & L_{2422} & L_{2433} & \sqrt{2}L_{2423} & \sqrt{2}L_{2431} & \sqrt{2}L_{2412} & L_{2441} & L_{2442} & L_{2443} \\ L_{3411} & L_{3422} & L_{3433} & \sqrt{2}L_{3423} & \sqrt{2}L_{3431} & \sqrt{2}L_{3412} & L_{3441} & L_{3442} & L_{3443} \end{bmatrix} \tag{30}$$

$$\langle \boldsymbol{S} \rangle^{\text{Mandel}} = \begin{bmatrix} S_{1111} & S_{1122} & S_{1133} & \sqrt{2}S_{1123} & \sqrt{2}S_{1131} & \sqrt{2}S_{1112} & S_{1141} & S_{1142} & S_{1143} \\ S_{2211} & S_{2222} & S_{2233} & \sqrt{2}S_{2223} & \sqrt{2}S_{2231} & \sqrt{2}S_{2212} & S_{2241} & S_{2242} & S_{2243} \\ S_{3311} & S_{3322} & S_{3333} & \sqrt{2}S_{3323} & \sqrt{2}S_{3331} & \sqrt{2}S_{3312} & S_{3341} & S_{3342} & S_{3343} \\ \sqrt{2}S_{2311} & \sqrt{2}S_{2322} & \sqrt{2}S_{2333} & 2S_{2323} & 2S_{2331} & 2S_{2312} & \sqrt{2}S_{2341} & \sqrt{2}S_{2342} & \sqrt{2}S_{2343} \\ \sqrt{2}S_{3111} & \sqrt{2}S_{3122} & \sqrt{2}S_{3133} & 2S_{3123} & 2S_{3131} & 2S_{3112} & \sqrt{2}S_{3141} & \sqrt{2}S_{3142} & \sqrt{2}S_{3143} \\ \sqrt{2}S_{1211} & \sqrt{2}S_{1222} & \sqrt{2}S_{1233} & 2S_{1223} & 2S_{1231} & 2S_{1212} & \sqrt{2}S_{1241} & \sqrt{2}S_{1242} & \sqrt{2}S_{1243} \\ S_{4111} & S_{4122} & S_{4133} & \sqrt{2}S_{4123} & \sqrt{2}S_{4131} & \sqrt{2}S_{4112} & S_{4141} & S_{4142} & S_{4143} \\ S_{4211} & S_{4222} & S_{4233} & \sqrt{2}S_{4223} & \sqrt{2}S_{4231} & \sqrt{2}S_{4212} & S_{4241} & S_{4242} & S_{4243} \\ S_{4311} & S_{4322} & S_{4333} & \sqrt{2}S_{4323} & \sqrt{2}S_{4331} & \sqrt{2}S_{4312} & S_{4341} & S_{4342} & S_{4343} \end{bmatrix}$$

$$\langle \boldsymbol{M} \rangle^{\text{Mandel}} = \begin{bmatrix} M_{1111} & M_{1122} & M_{1133} & \sqrt{2}M_{1123} & \sqrt{2}M_{1131} & \sqrt{2}M_{1112} & M_{1141} & M_{1142} & M_{1143} \\ M_{2211} & M_{2222} & M_{2233} & \sqrt{2}M_{2223} & \sqrt{2}M_{2231} & \sqrt{2}M_{2212} & M_{2241} & M_{2242} & M_{2243} \\ M_{3311} & M_{3322} & M_{3333} & \sqrt{2}M_{3323} & \sqrt{2}M_{3331} & \sqrt{2}M_{3312} & M_{3341} & M_{3342} & M_{3343} \\ \sqrt{2}M_{2311} & \sqrt{2}M_{2322} & \sqrt{2}M_{2333} & 2M_{2323} & 2M_{2331} & 2M_{2312} & \sqrt{2}M_{2341} & \sqrt{2}M_{2342} & \sqrt{2}M_{2343} \\ \sqrt{2}M_{3111} & \sqrt{2}M_{3122} & \sqrt{2}M_{3133} & 2M_{3123} & 2M_{3131} & 2M_{3112} & \sqrt{2}M_{3141} & \sqrt{2}M_{3142} & \sqrt{2}M_{3143} \\ \sqrt{2}M_{1211} & \sqrt{2}M_{1222} & \sqrt{2}M_{1233} & 2M_{1223} & 2M_{1231} & 2M_{1212} & \sqrt{2}M_{1241} & \sqrt{2}M_{1242} & \sqrt{2}M_{1243} \\ M_{1411} & M_{1422} & M_{1433} & \sqrt{2}M_{1423} & \sqrt{2}M_{1431} & \sqrt{2}M_{1412} & M_{1441} & M_{1442} & M_{1443} \\ M_{2411} & M_{2422} & M_{2433} & \sqrt{2}M_{2423} & \sqrt{2}M_{2431} & \sqrt{2}M_{2412} & M_{2441} & M_{2442} & M_{2443} \\ M_{3411} & M_{3422} & M_{3433} & \sqrt{2}M_{3423} & \sqrt{2}M_{3431} & \sqrt{2}M_{3412} & M_{3441} & M_{3442} & M_{3443} \end{bmatrix},$$

As shown in Eq. (30), all the transformed matrices have identical coefficients, $\sqrt{2}$ or 2, regardless of the tensor type. Using the Mandel notation, one can evaluate Eq. (26) by carrying out 9×9 matrix calculations. Thus, the modified Eshelby tensor can be obtained as

$$\langle \boldsymbol{S}^M \rangle^{\text{Mandel}} = \left(\langle \boldsymbol{I} \rangle^{\text{Mandel}} + \langle \boldsymbol{\Gamma} \rangle^{\text{Mandel}} \right)^{-1} \left(\langle \boldsymbol{S} \rangle^{\text{Mandel}} + \langle \boldsymbol{\Gamma} \rangle^{\text{Mandel}} \right) \tag{31}$$

It is notable that the Eq. (31) can not be obtained by using the Voigt notation. For example, let $\boldsymbol{Q} = \boldsymbol{S} : \boldsymbol{L}$ $\left(Q_{MnRs} = S_{MnJq} L_{qJRs} \right)$, then Q_{2323} is expressed as follows:

$$\begin{aligned} Q_{2323} = {} & S_{2311}L_{1123} + S_{2322}L_{2223} + S_{2333}L_{3323} + 2S_{2323}L_{2323} + 2S_{2331}L_{3123} \\ & + 2S_{2312}L_{1223} + S_{2341}L_{1423} + S_{2342}L_{2423} + S_{2343}L_{3423} \end{aligned} \tag{32}$$

Eq. (32) is rewritten by using the Voigt and Mandel notation and Eq. (34) satisfies $\langle \boldsymbol{Q} \rangle_{44}^{\text{Mandel}} = 2Q_{2323} = \langle \boldsymbol{S} \rangle_{4K}^{\text{Mandel}} \langle \boldsymbol{L} \rangle_{K4}^{\text{Mandel}}$ whereas Eq. (33) does not satisfy $Q_{2323} = k \langle \boldsymbol{S} \rangle_{4K}^{\text{Voigt}} \langle \boldsymbol{L} \rangle_{K4}^{\text{Voigt}}$, where k is constant.

$$Q_{2323} = \frac{1}{2}\langle \boldsymbol{S} \rangle_{41}^{\text{Voigt}} \langle \boldsymbol{L} \rangle_{14}^{\text{Voigt}} + \frac{1}{2}\langle \boldsymbol{S} \rangle_{42}^{\text{Voigt}} \langle \boldsymbol{L} \rangle_{24}^{\text{Voigt}} + \frac{1}{2}\langle \boldsymbol{S} \rangle_{43}^{\text{Voigt}} \langle \boldsymbol{L} \rangle_{34}^{\text{Voigt}}$$
$$+ \langle \boldsymbol{S} \rangle_{44}^{\text{Voigt}} \langle \boldsymbol{L} \rangle_{44}^{\text{Voigt}} + \langle \boldsymbol{S} \rangle_{45}^{\text{Voigt}} \langle \boldsymbol{L} \rangle_{54}^{\text{Voigt}} + \langle \boldsymbol{S} \rangle_{46}^{\text{Voigt}} \langle \boldsymbol{L} \rangle_{64}^{\text{Voigt}} \tag{33}$$
$$+ \frac{1}{2}\langle \boldsymbol{L} \rangle_{47}^{\text{Voigt}} \langle \boldsymbol{S} \rangle_{74}^{\text{Voigt}} + \frac{1}{2}\langle \boldsymbol{L} \rangle_{48}^{\text{Voigt}} \langle \boldsymbol{S} \rangle_{84}^{\text{Voigt}} + \frac{1}{2}\langle \boldsymbol{L} \rangle_{49}^{\text{Voigt}} \langle \boldsymbol{S} \rangle_{94}^{\text{Voigt}}$$

$$Q_{2323} = \frac{1}{2}\langle \boldsymbol{S} \rangle_{41}^{\text{Mandel}} \langle \boldsymbol{L} \rangle_{14}^{\text{Mandel}} + \frac{1}{2}\langle \boldsymbol{S} \rangle_{42}^{\text{Mandel}} \langle \boldsymbol{L} \rangle_{24}^{\text{Mandel}} + \frac{1}{2}\langle \boldsymbol{S} \rangle_{43}^{\text{Mandel}} \langle \boldsymbol{L} \rangle_{34}^{\text{Mandel}}$$
$$+ \frac{1}{2}\langle \boldsymbol{S} \rangle_{44}^{\text{Mandel}} \langle \boldsymbol{L} \rangle_{44}^{\text{Mandel}} + \frac{1}{2}\langle \boldsymbol{S} \rangle_{45}^{\text{Mandel}} \langle \boldsymbol{L} \rangle_{54}^{\text{Mandel}}$$
$$+ \frac{1}{2}\langle \boldsymbol{S} \rangle_{46}^{\text{Mandel}} \langle \boldsymbol{L} \rangle_{64}^{\text{Mandel}} + \frac{1}{2}\langle \boldsymbol{L} \rangle_{47}^{\text{Mandel}} \langle \boldsymbol{S} \rangle_{74}^{\text{Mandel}} \tag{34}$$
$$+ \frac{1}{2}\langle \boldsymbol{L} \rangle_{48}^{\text{Mandel}} \langle \boldsymbol{S} \rangle_{84}^{\text{Mandel}} + \frac{1}{2}\langle \boldsymbol{L} \rangle_{49}^{\text{Mandel}} \langle \boldsymbol{S} \rangle_{94}^{\text{Mandel}}$$
$$= \frac{1}{2}\langle \boldsymbol{S} \rangle_{4K}^{\text{Mandel}} \langle \boldsymbol{L} \rangle_{K4}^{\text{Mandel}}$$

We calculate the modified Eshelby tensor for PZT-5A with the material constants listed in Table 1. When conventional units are used, (the unit of the elastic constants is GPa = 10^9 Pa and that of the piezoelectric constants is C/m^2), numerical errors are likely to accumulate during the matrix inverse operation due to the significant difference in the order of magnitudes between the two constants. To avoid the numerical error, we set the unit of charge as nC = 10^{-9} C (Ryu et al., 2019).

2.5 Numerical validation

To validate the modified Eshelby tensor results, we carry out a series of FEA simulations using COMSOL (Comsol, 2015). We use a single inclusion with diameter of 2 mm and a matrix in cubic shape with edge length of 20 mm (the edge length is ten times longer than the diameter of the inclusion to reduce the effect of the finite size as seen as Fig.

3). We use approximately 400,000 and 8,000 3D linear tetrahedron elements to construct the mesh inside the matrix and inclusion, respectively. The unit eigenstrain is assigned on the inclusion under the fixed outer surfaces of the matrix, and we then predict the Eshelby tensor using the constrained strain and electric field.

We predict the modified Eshelby tensor for a wide range of interfacial ranges and compare the result with FEA calculations as depicted in Fig. 4. Fig. 4(a)–(c) shows the modified Eshelby tensor when only elastic interfacial damage is considered ($\alpha = \beta \neq 0, \gamma = 0$). As α goes to infinite, the traction converges to zero, so the inclusion deforms by eigenstrain ($\boldsymbol{Z} = \boldsymbol{Z}^*$), which implies that $S^M_{1111} = 1, S^M_{2211} = S^M_{4311} = 0$. Further, when the electric interfacial damage increases in the absence of an elastic interfacial damage, S^M_{4311} decreases and converges to a finite value at an infinite electric interfacial damage (Fig. 4(d)). Even in the infinite electric interfacial damage limit, the strain field around the inclusion is finite because there is no elastic interfacial damage. Hence, the finite electric field within the inclusion is induced by the piezoelectric effect, i.e., it is due to the charge accumulated at the matrix side of the interface. With the increase in the elastic interfacial damage (the $\alpha_0 = 1.21$ case in Fig. 4(d)), the electric field within the inclusion reduces because of the reduction in the strain field around the inclusion. We note that, in the limit of the infinite interfacial damage for both (i.e., $\alpha = \beta \to \infty,\ \gamma \to \infty$), all diagonal components converge to 1 and the off-diagonal terms go to zero because of the complete mechanical and electric decoupling between the inclusion and the matrix. The result can be evidently explained with Eq. (31). When the interfacial damage increases, $\boldsymbol{\Gamma}$ goes to infinite and $\langle \boldsymbol{S}^M \rangle^{\text{Mandel}}$ converges to the 9×9 identity matrix.

3. Modified strain concentration tensor

3.1 Single inhomogeneity problem

When the extended strain $(\boldsymbol{Z}^0)$ is applied to the infinite matrix $(\boldsymbol{L}_0)$ having single inhomogeneity $(\boldsymbol{L}_1)$, the extended strain field within the inhomogeneity $(\boldsymbol{Z}_1)$ can be obtained by using the superposition principle. When the interfacial damage is absent, the problem is decomposed into two homogeneous problems (Dunn and Taya, 1993a, c). The first problem is the homogeneous material $(\boldsymbol{L}_0)$ under the applied extended strain $(\boldsymbol{Z}^0)$, and its solution is given as a uniform strain field, equal to the applied extended strain, over the entire region. The second problem is the single inclusion problem having an equivalent eigenstrain expressed as

$$\boldsymbol{Z}^{Eq} = -[(\boldsymbol{L}_1 - \boldsymbol{L}_0)\colon \boldsymbol{S} + \boldsymbol{L}_0]^{-1}\colon (\boldsymbol{L}_1 - \boldsymbol{L}_0)\colon \boldsymbol{Z}^0. \tag{35}$$

After superposing the solutions, the extended strain field within the inhomogeneity is obtained as follows:

$$\begin{aligned} \boldsymbol{Z}_1 &= \boldsymbol{Z}^{\boldsymbol{I}} + \boldsymbol{Z}^{\boldsymbol{II}} = \boldsymbol{Z}^{\boldsymbol{0}} + \boldsymbol{S}\colon \boldsymbol{Z}^{\boldsymbol{Eq}} \\ &= [\boldsymbol{I} + \boldsymbol{S}\colon \boldsymbol{L}_0^{-1}\colon (\boldsymbol{L}_1 - \boldsymbol{L}_0)]^{-1}\colon \boldsymbol{Z}^0 \end{aligned} \tag{36}$$

In the presence of the interfacial damage, an additional interfacial contribution due to the extended displacement should be inserted as the 3rd contribution (Fig. 5),

$$\boldsymbol{Z}^{\boldsymbol{III}} = -\boldsymbol{\Gamma}\colon (\boldsymbol{Z}_{\boldsymbol{1}} - \boldsymbol{Z}^{\boldsymbol{Eq}}). \tag{37}$$

We note that the previous studies obtained the modified strain concentration tensor, simply by replacing the Eshelby tensor in Eq. (36) with the modified Eshelby tensor, which results in a mismatching boundary condition at the interface (Wang et al., 2014a; Wang et al., 2014c). We have pointed out and corrected similar errors in the micromechanics studies on elasticity (Lee et al., 2019a; Lee et al., 2019b) and heat conduction (Lee et al., 2018). Finally, the extended

strain field within the single inhomogeneity is expressed as

$$\begin{aligned} \boldsymbol{Z_1} &= \boldsymbol{Z^I} + \boldsymbol{Z^{II}} + \boldsymbol{Z^{III}} = \boldsymbol{Z^0} + \boldsymbol{S}\colon \boldsymbol{Z^{Eq}} - \boldsymbol{\Gamma}\colon (\boldsymbol{Z_1} - \boldsymbol{Z^{Eq}}) \\ &= \left(\boldsymbol{I} + \boldsymbol{S}\colon \boldsymbol{L_0^{-1}}\colon (\boldsymbol{L_1} - \boldsymbol{L_0}) + \boldsymbol{\Gamma}\colon \boldsymbol{L_0^{-1}}\colon \boldsymbol{L_1}\right)\colon \boldsymbol{Z^0} \\ &= \boldsymbol{A^M}\colon \boldsymbol{Z^0} \end{aligned} \tag{38}$$

In the limit of zero interfacial damage, Eq. (38) converges to the strain concentration tensor for perfect interface in Eq. (36).

3.2 Numerical validation

To validate Eq. (38), we compare the theoretical predictions with the FEA results by considering a composite having SiC reinforcement and PVDF matrix. The material properties of each phase are listed in Table 1, and the mesh configuration is the same as that the single inclusion problem (Fig. 3). The Mandel notation is used to carry out tensor operations. As shown in Fig. 6, our predictions match well with the FEA results for a wide range of interfacial damages. For a comparison, we also plot the modified concentration tensor obtained by replacing the Eshelby tensor in Eq. (36) with the modified Eshelby tensor in Eq. (26), which deviates significantly from the correct value in the entire range of interfacial damages.

In the absence of electric interfacial imperfection ($\gamma_0 = 0$), A^M_{3333}, which refers to the ratio between the 33 strain components inside the inhomogeneity and the far field 33 strains, converges to zero in the very large interfacial elastic compliance limit ($\alpha_0 \to \infty$) as shown in Fig. 6(a), because more strain energy is stored at the interfacial spring with increasing interfacial compliance. The same behavior occurs for other A^M_{ijkl} components concerning the relation between elastic strains (i.e. $i, j, k, l \leq 3$). Besides, A^M_{4333} (the ratio

between the interior electric field along the 3rd axis and the applied 33 strains at the far field) remains finite in the limit of infinite interfacial compliance $\alpha_0 \to \infty$ (with $\gamma_0 = 0$) as depicted in Fig. 6(b). Because the strain field distribution in the piezoelectric PVDF matrix does not converge to zero but becomes identical to the strain field of a matrix having a spherical cavity, the finite surface charge accumulated at the piezoelectric matrix side of the interface produces a uniform electric field inside the SiC reinforcement, even in the $\alpha_0 \to \infty$ limit. When the interfacial electric imperfection γ_0 is present, A^M_{4333} reduces and eventually approaches to zero in the $\gamma_0 \to \infty$ limit. The same trend is observed for the all components of the interior electric field regardless of applied loading type (mechanical strain or electric field), i.e., A^M_{4jKl} decreases monotonically with increasing γ_0 and converges to zero as $\gamma_0 \to \infty$ (Fig. 6(b)–(d)).

4. Effective properties of piezoelectric composite

4.1 The Mori–Tanaka method and FEA condition

Based on the Mori-Tanaka method, we predict the effective modulus of the SiC particle reinforced PVDF composite with corrected modified Eshelby tensor and strain concentration tensor. The effective piezoelectric moduli tensor (Wang et al., 2014a; Wang et al., 2014c) of the composite having spring-type interfacial damage is expressed as

$$\boldsymbol{L^{\mathrm{Eff}}} = (c_0\boldsymbol{L_0} + c_1\boldsymbol{L_1}\colon\boldsymbol{A^M})\colon(c_0\boldsymbol{I} + c_1\boldsymbol{A^M} + c_1\boldsymbol{R}\colon\boldsymbol{L_1}\colon\boldsymbol{A^M})^{-1} \tag{39}$$

where c_0 and c_1 denote the volume fraction of the matrix and particle, respectively so $c_0 + c_1 = 1$. $\boldsymbol{R}$ represents the intensity of the interfacial damage, which is expressed as

$$R_{MnJq} = \frac{\omega^J}{a} I_{MnJq}, \qquad \langle\boldsymbol{R}\rangle^{\mathrm{Mandel}} = \frac{1}{a}\begin{bmatrix} \alpha & & & & & & & & \\ & \alpha & & & & & & & \\ & & \alpha & & & & & & \\ & & & \alpha & & & & & \\ & & & & \alpha & & & & \\ & & & & & \alpha & & & \\ & & & & & & -\gamma & & \\ & & & & & & & -\gamma & \\ & & & & & & & & -\gamma \end{bmatrix} \tag{40}$$

Using the effective modulus, we can predict the extended strain/stress field within each phase. The applied extended strain $(\overline{\boldsymbol{Z}})$ and stress $(\overline{\boldsymbol{\Sigma}})$ for a composite can be written in terms of the volume averaged extended strain $\overline{\boldsymbol{Z}}_{\boldsymbol{i}}$ and stress field $\overline{\boldsymbol{\Sigma}}_{\boldsymbol{i}}$ within each phase as

$$\begin{aligned} \overline{\boldsymbol{Z}} &= c_0\overline{\boldsymbol{Z}}_{\boldsymbol{0}} + c_1\overline{\boldsymbol{Z}}_{\boldsymbol{1}} + c_1\boldsymbol{R}\colon\boldsymbol{L_1}\colon\overline{\boldsymbol{Z}}_{\boldsymbol{1}} \\ \overline{\boldsymbol{\Sigma}} &= c_0\overline{\boldsymbol{\Sigma}}_{\boldsymbol{0}} + c_1\overline{\boldsymbol{\Sigma}}_{\boldsymbol{1}} \end{aligned} \tag{41}$$

We can rewrite the stress equation in Eq. (41) as

$$\boldsymbol{L^{\mathrm{eff}}}\overline{\boldsymbol{Z}} = c_0\boldsymbol{L_0}\colon\overline{\boldsymbol{Z}}_{\boldsymbol{0}} + c_1\boldsymbol{L_1}\colon\overline{\boldsymbol{Z}}_{\boldsymbol{1}}. \tag{42}$$

Hence, the strain and stress field within each phase are expressed as Eq. (43) and (44), respectively.

$$\overline{\boldsymbol{Z}}_{\boldsymbol{0}} = \frac{1}{c_0}(\boldsymbol{L_0} - \boldsymbol{L_1}\colon(\boldsymbol{I} + \boldsymbol{R}\colon\boldsymbol{L_1})^{-1})^{-1}\colon\left(\boldsymbol{L}^{\mathbf{eff}} - \boldsymbol{L_1}\colon(\boldsymbol{I} + \boldsymbol{R}\colon\boldsymbol{L_1})^{-1}\right)$$
$$\overline{\boldsymbol{Z}}_{\boldsymbol{1}} = \frac{1}{c_1}(\boldsymbol{L_1} - \boldsymbol{L_0}\colon(\boldsymbol{I} + \boldsymbol{R}\colon\boldsymbol{L_1})^{-1})^{-1}\colon\left(\boldsymbol{L}^{\mathbf{eff}} - \boldsymbol{L_0}\right) \quad (43)$$

$$\overline{\boldsymbol{\Sigma}}_{\boldsymbol{0}} = \frac{1}{c_0}(\boldsymbol{M_0} - \boldsymbol{M_1} - \boldsymbol{R})^{-1}\colon\left(\boldsymbol{M}^{\mathbf{eff}} - \boldsymbol{M_1} - \boldsymbol{R}\right)$$
$$\overline{\boldsymbol{\Sigma}}_{\boldsymbol{1}} = \frac{1}{c_1}(\boldsymbol{M_1} - \boldsymbol{M_0} + \boldsymbol{R})^{-1}\colon\left(\boldsymbol{M}^{\mathbf{eff}} - \boldsymbol{M_0}\right) \quad (44)$$

For the validation of the theoretical predictions, we calculate the effective modulus of the particle reinforced representative volume element (RVE) using FEA. We construct RVEs having about 20 particles and calculate the average effective modulus of 10 independent RVEs with a different particle distribution to obtain a statistically meaningful value (Fig. 7). To obtain the effective piezoelectric modulus, we calculate the ratio between the volume averaged stress/electric displacement field and the applied unit strain/electric field.

4.2 Effective properties of composite having one type of interfacial damages

First, we show the effect of elastic interfacial damage on the effective modulus, dielectric constant, and piezoelectric constant of SiC-PVDF composites with two different volume fractions in Fig. 8. The effective modulus predicted with our modified Eshelby tensor and strain concentration tensor matches well with the FEA results up to 10% volume fraction, showing a relative error less than 2% (Fig. 8(a)). In the small interfacial damage regime, the elastic stiffness of a composite with high volume fraction is higher than that of a composite having low volume fraction because the composite is stiffened with additional SiC particles. However, as the interfacial damage increases, the stiffness of a composite with higher SiC volume fraction decreases compared with that of a composite with lower SiC volume fraction, because SiC effectively serves as a soft inhomogeneity when the load transfer between the SiC particle and the PVDF matrix is excessively weakened. As the elastic interfacial damage

approaches infinity, the predicted modulus converges to the porous matrix result (whereas the prediction from the previous study converges to zero) (Fig. 8(f)). The effective piezoelectric constant ($-e_{333}$) also decreases as the elastic interfacial damage increases whereas the effective dielectric constant was not significantly affected by the elastic interfacial damage (Fig. 8(b) and (c)). To understand the origin of decrease in the effective piezoelectric constant, we plot the volume averaged strain of each phase in Fig. 8(d). The volume averaged strain within both matrix and particles decrease with the increase in the interfacial damage, because the interfacial spring extends more with increasing spring compliance, which leads to reduced charge induction from the piezoelectric matrix (Fig. 8(e)). In the infinitely large elastic interfacial damage without electric interfacial damage, the composite has higher effective piezoelectric constant than that of the porous material because the SiC particle is also polarized owing to the finite interior electric field (Fig. 8(g)).

Second, we present the effective properties of the composite in the presence of the electric interface damage (Fig. 9). For a small electric interfacial damage, the effective dielectric constant κ_{33} increases with the SiC volume fraction because the dielectric constant of SiC is larger than that of the PVDF matrix. At a large electric interfacial damage, a composite with higher volume fraction of SiC particles has lower effective dielectric constant because the SiC particles are not polarized effectively. When the electric interfacial damage approaches infinity, the effective dielectric constant decreases below the dielectric constant of the porous matrix (Fig. 9(a) and (f)). This is because while the infinite electric interfacial electric damage indicates zero electric field within the SiC particle, the porous material with vacuum or air voids can have a finite electric field within the void.

This is different from the elasticity or heat conduction problems reported in the previous studies (Lee et al., 2019a; Lee et al., 2018) where the effective property of a

composite in the infinite interfacial damage limit is equal to the effective property of a porous matrix. At infinite interfacial damage, the Mori–Tanaka method with the interface spring model converges to the results obtained with the material properties of a particle set to be zero. In elasticity and heat conduction, the elastic stiffness and thermal conductivity of the void (vacuum) are zero, so the two results (porous and infinite interfacial damage) become identical. However, when addressing the dielectric response, given that the vacuum void has unit relative permittivity (i.e., $\kappa_{ij} = \delta_{ij}$), the effective dielectric constant at infinite electric interfacial damage is lower than that of a porous material.

The effective stiffness is almost constant regardless of the electric interfacial damage and the effective piezoelectric constant $(-e_{333})$ decreases as the interfacial electric damage increases (Fig. 9(b) and (c)). When the electric field is applied to the composite, the electric field within the matrix decreases with the interfacial electric compliance γ (See Fig. 9(d) and (e)). Therefore, less mechanical strain is induced from the piezoelectric matrix, which implies a decreased $-e_{333}$, and owing to the mechanically "tie" condition at the interface(i.e. $\alpha = 0$), the $-e_{333}$ at infinitely large γ is larger than the lower limit (Fig. 9(g)).

4.3 Effective properties of composite having two types of interfacial damages.

We also predict the effective properties of the composite having both types of interfacial damages. Fig. 10 shows that the effective stiffness mostly depends on the elastic interfacial damage, and it decreases with an increase in elastic interfacial damage, as expected. Our prediction had the maximum error of 0.78% compared with the FEA results. Similarly, the effective dielectric constant is affected mostly by the electric interfacial damage. However, the effective $-e_{333}$ depends on both interfacial damages because it considers the coupling between mechanical and electrical responses. As the two interfacial damages simultaneously approach infinity, the effective piezoelectric and dielectric constants become

lower than the porous results, whereas the effective stiffness converges to almost the same modulus as that with a porous material (Fig. 10(d)–(f)). Here, we use the normalized interfacial damage parameter ($\alpha_0 = \alpha C^0_{1111}/a,\ \gamma_0 = \gamma\kappa^0_{11}/a$); thus, the small size of the particle results in a large normalized interfacial damage. Hence, the effective properties depend on the size of SiC particles at fixed α and γ (Appendix C).

Then, we obtain the figure of merit in 33 directions (FOM_{33}) by predicting the effective d_{333} and κ^{σ}_{33} in the strain-charge form constitutive equation,

$$\begin{aligned} \boldsymbol{\varepsilon} &= \boldsymbol{C}^{-1}\!:\boldsymbol{\sigma} + \boldsymbol{d}^{T}\cdot\boldsymbol{E} \\ \boldsymbol{D} &= \boldsymbol{d}\!:\boldsymbol{\sigma} + \boldsymbol{\kappa}^{\boldsymbol{\sigma}}\cdot\boldsymbol{E}. \end{aligned} \tag{45}$$

We predict the effective $-d_{333}$ in terms of both electric and elastic interfacial damage (Fig. 11). The effective $-d_{333}$ decreases with an increase in the electrical damage, whereas it increases as the elastic interfacial damage increases. As expressed in Eq. (37), when an external stress is applied, the stress field within the matrix increases with the elastic interfacial damage because the average stress field within the particles approaches zero (Fig. 11(b)). Using the κ^{σ}_{33} shown in Fig. 11, we predict the effective FOM_{33} by using Eq. (42).

$$FOM_{33} = \frac{(d_{333})^2}{\kappa^{\sigma}_{33}} \tag{46}$$

As shown in Fig. 11, the effective FOM_{33} increases with both interfacial damages. At a large interfacial damage, FOM_{33} is even higher than that of the pure matrix. This is similar to the porous material results studied by other researchers (Dunn and Taya, 1993b; Zhang et al., 2017). For a porous material, the effective FOM_{33} increases with porosity because κ^{σ}_{33} decreases more rapidly than $(d_{333})^2$ with respect to the porosity. Similar to a porous material, a composite with a piezoelectric matrix and elastic particles has high FOM_{33} when the interfacial damage is large.

5. Conclusion

We predict the effective material properties of a piezoelectric composite, considering the elastic and electric interfacial damage. We derive the modified Eshelby tensor after correcting the equations used in previous studies and validate it by comparison with the FEA results for a wide range of two interfacial damages. We also correctly predict the modified extended strain concentration tensor by decomposing the single inhomogeneity problem into three independent homogeneous problems. Using the modified Eshelby tensor and extended strain concentration tensor, we predict the effective properties of the reinforced composite, and note that our model agrees well with the FEA results up to a 10% volume fraction. The effective moduli are well bounded between two limit cases, perfect bonding and porous results, except the effective dielectric constant. We suggest a 2D map of effective properties with respect to the two interfacial damage parameters.

Acknowledgements

This research was supported by the Basic Science Program(NRF-2019R1A2C4070690), the Creative Materials Discovery Program(NRF-2016M3D1A1900038), and the International Research & Development Program(NRF-2018K2A9A2A12000223) of the National Research Foundation of Korea(NRF) funded by the Ministry of Science and ICT of Korea.

Appendix A. Non-uniform strain field within the inclusion.

The extended strain field within the inclusion in non-uniform when the elastic interfacial spring compliance in normal and tangential direction are different. As shown in Fig. A1, the strain field of spherical inclusion is non-uniform whereas the strain field when $\alpha = \beta$ is uniform. For ellipsoidal case, the strain field is nonuniform even if the spring compliances are same.

Appendix B. Violation of Fubini-Tonelli theorem

In this section, we explain the violation of Fubini-Tonelli theorem by suggesting a simple double integral problem. When the integral function has singularity within the integral domain, the order of integral can not be exchanged. For example, for the function

$$\frac{x^2-y^2}{(x^2+y^2)^2} = -\frac{\partial^2}{\partial x \partial y}\arctan(y/x), \tag{B.1}$$

the results of two integrals which has different integral order are different, as shown in Eq.(B.2)

$$\begin{aligned} \int_0^1 \left(\int_0^1 \frac{x^2-y^2}{(x^2+y^2)^2} dy \right) dx &= -\frac{\pi}{4} \\ \int_0^1 \left(\int_0^1 \frac{x^2-y^2}{(x^2+y^2)^2} dx \right) dy &= \frac{\pi}{4} \end{aligned} \tag{B.2}$$

Appendix C. Effect of particle size on effective properties

In the main text, we investigate the effect of interfacial damage on the effective properties using normalized interfacial damage, $\alpha_0 = \alpha C^0_{1111}/a,\ \gamma_0 = \gamma \kappa^0_{11}/a,$ where a is radius of the particle in the composite. If we predict the effective properties using interfacial damage, not normalized parameter, the effective properties decrease with the size of the particle (See Fig. C1). As the size of the particle decreases at a fixed volume fraction, the total interface area increases, which results in large interfacial damage, so the effective properties decrease.

Table 1 Material constants of the considered materials. The constants are obtained from the previous studies (Odegard, 2004; Wang et al., 2014c).

Property	PZT-5A	PVDF	SiC
C_{1111} (GPa)	121	3.8	483.7
C_{1122} (GPa)	75.4	1.9	99.1
C_{1133} (GPa)	75.2	1.0	99.1
C_{2222} (GPa)	121	3.2	483.7
C_{2233} (GPa)	75.2	0.9	99.1
C_{3333} (GPa)	111	1.2	483.7
C_{2323} (GPa)	21.1	0.7	192.3
C_{3131} (GPa)	21.1	0.9	192.3
C_{1212} (GPa)	2.28	0.9	192.3
e_{131} (C/m^2)	12.3	0.0	0.0
e_{311} (C/m^2)	-5.4	0.024	0.0
e_{322} (C/m^2)	-5.4	0.001	0.0
e_{333} (C/m^2)	15.8	-0.027	0.0
κ_1/κ_0	916	7.4	10.0
κ_2/κ_0	916	9.3	10.0
κ_3/κ_0	830	7.6	10.0

$\kappa_0 = 8.854187817 \times 10^{-12}$ C^2/Nm^2

Figures and captions

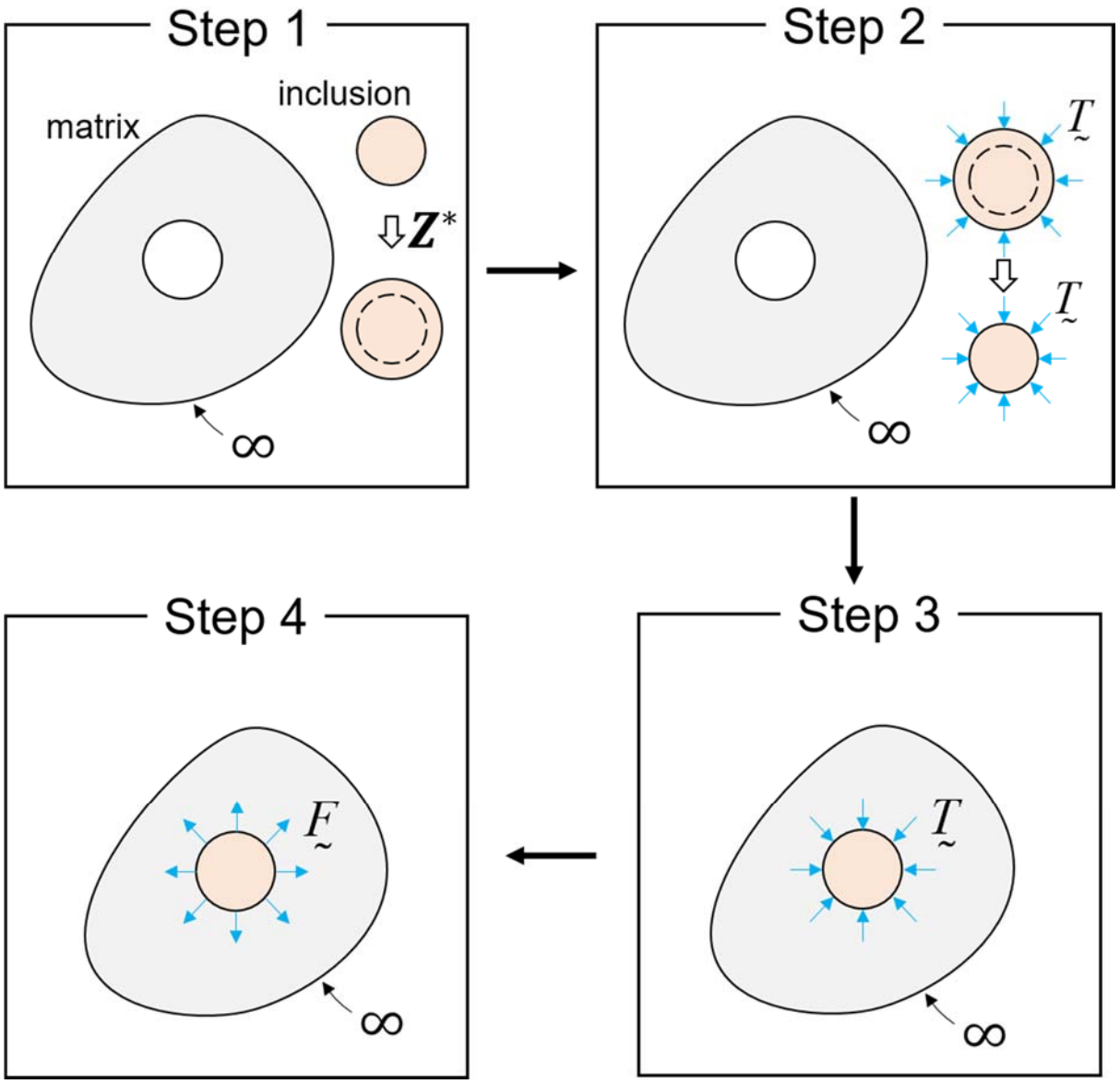

Fig. 1. Schematic of the single inclusion problem

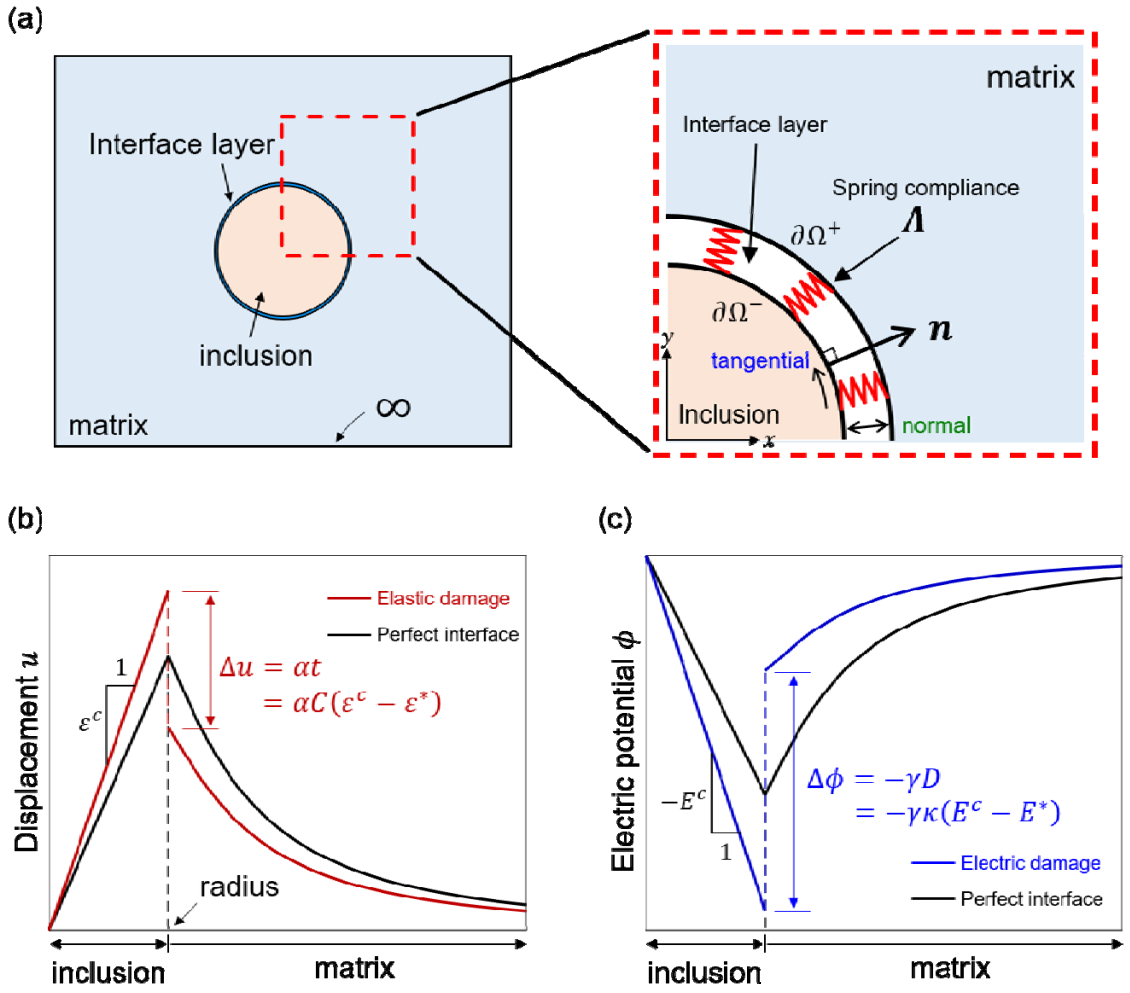

Fig. 2. (a) Schematic of the interface spring model. The right figure shows the deformed state having a finite (extended) displacement jump across the interface. Schematic representation of (b) displacement and (c) potential field of the single inclusion problem having interfacial damage.

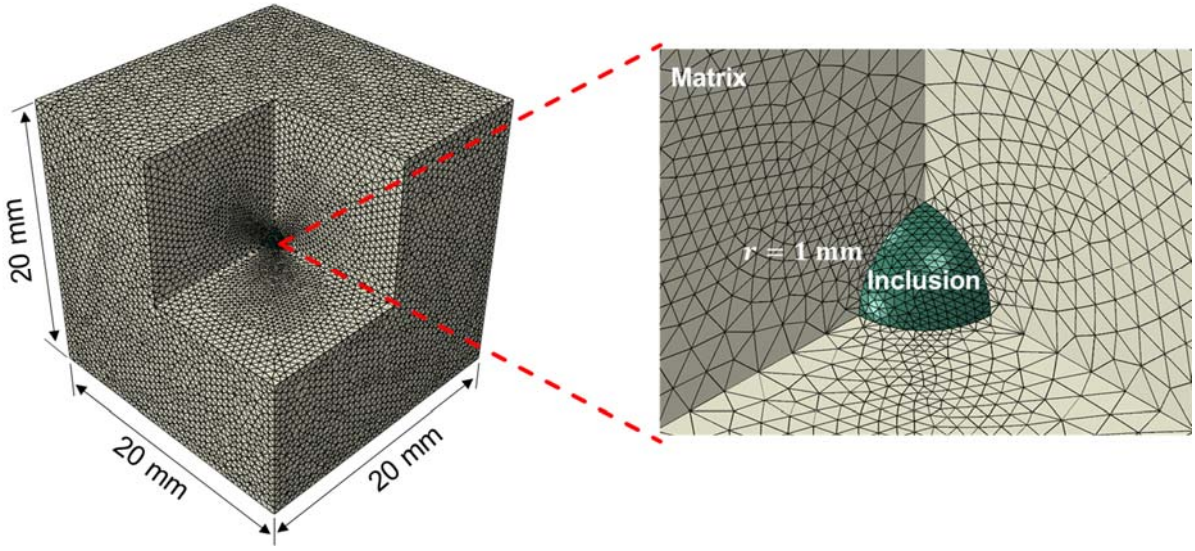

Fig. 3. Mesh configuration of the single inclusion/inhomogeneity problem.

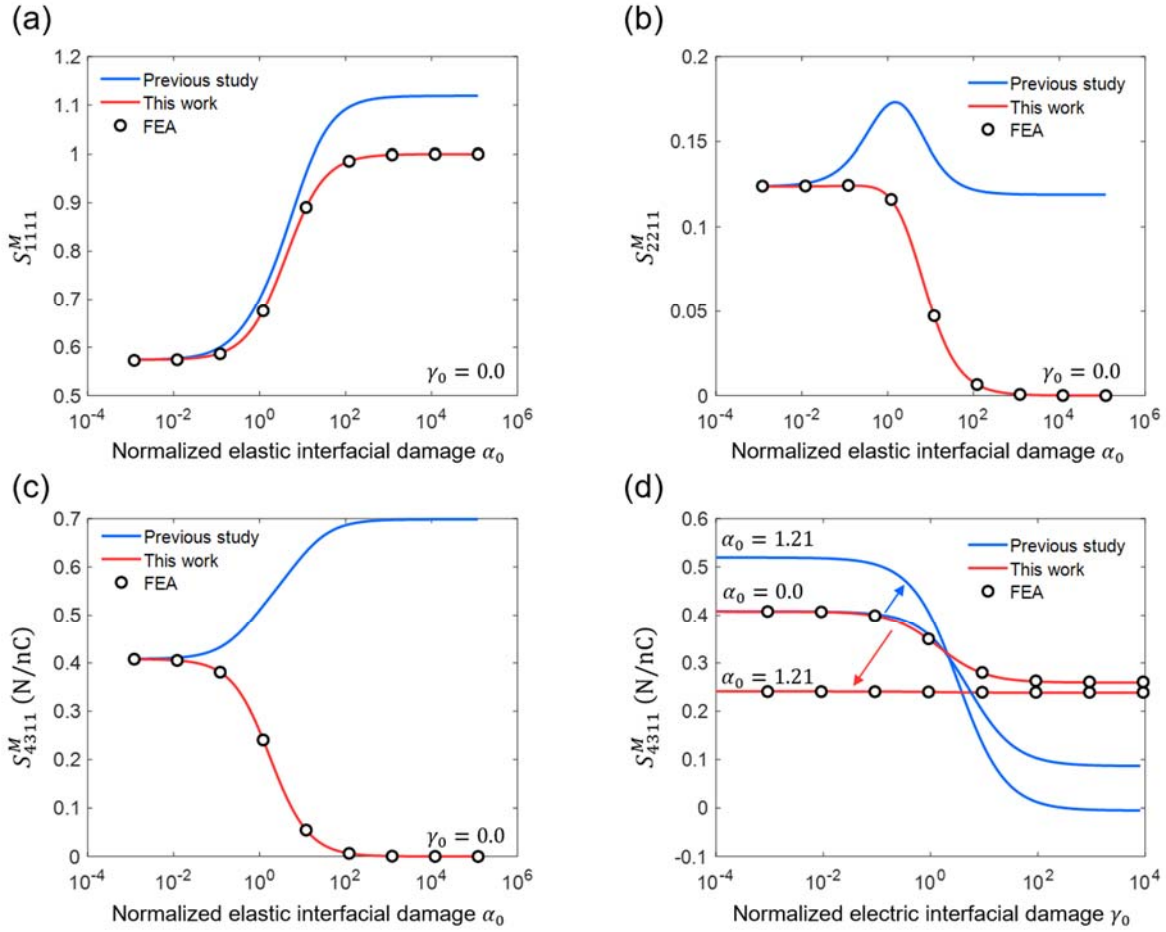

Fig. 4. (a) S^M_{1111}, (b) S^M_{2211}, and (c) S^M_{4311} as a function of the normalized elastic interfacial damage. (d) S^M_{4311} with respect to normalized electric interfacial damage. We normalized the interfacial damage by $\alpha_0 = C_{1111}\alpha/a$, $\gamma_0 = \kappa_{11}\gamma/a$. We also present the results obtained from equations used in the previous study (Wang et al., 2014c).

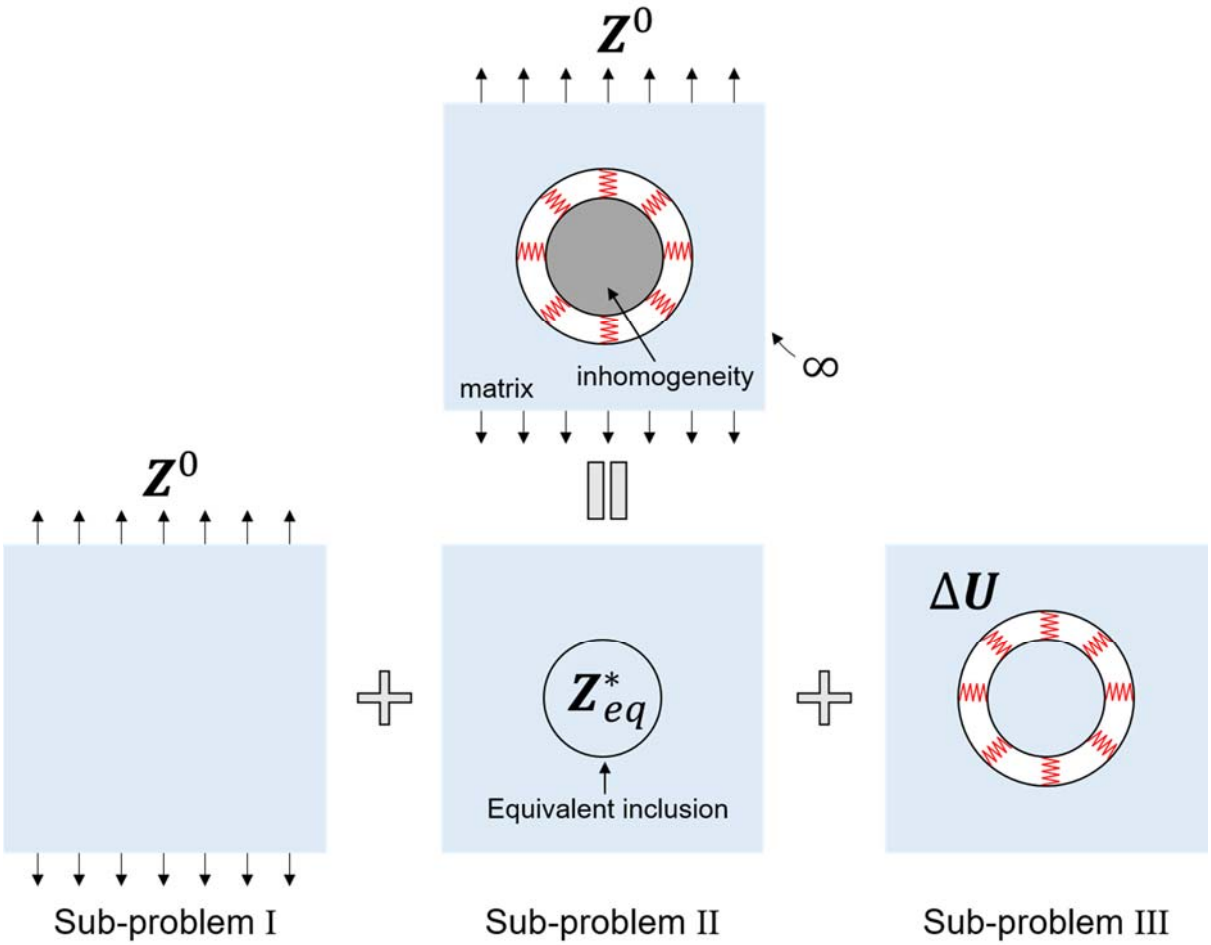

Fig. 5. Schematic of the single inhomogeneity problem having interface spring.

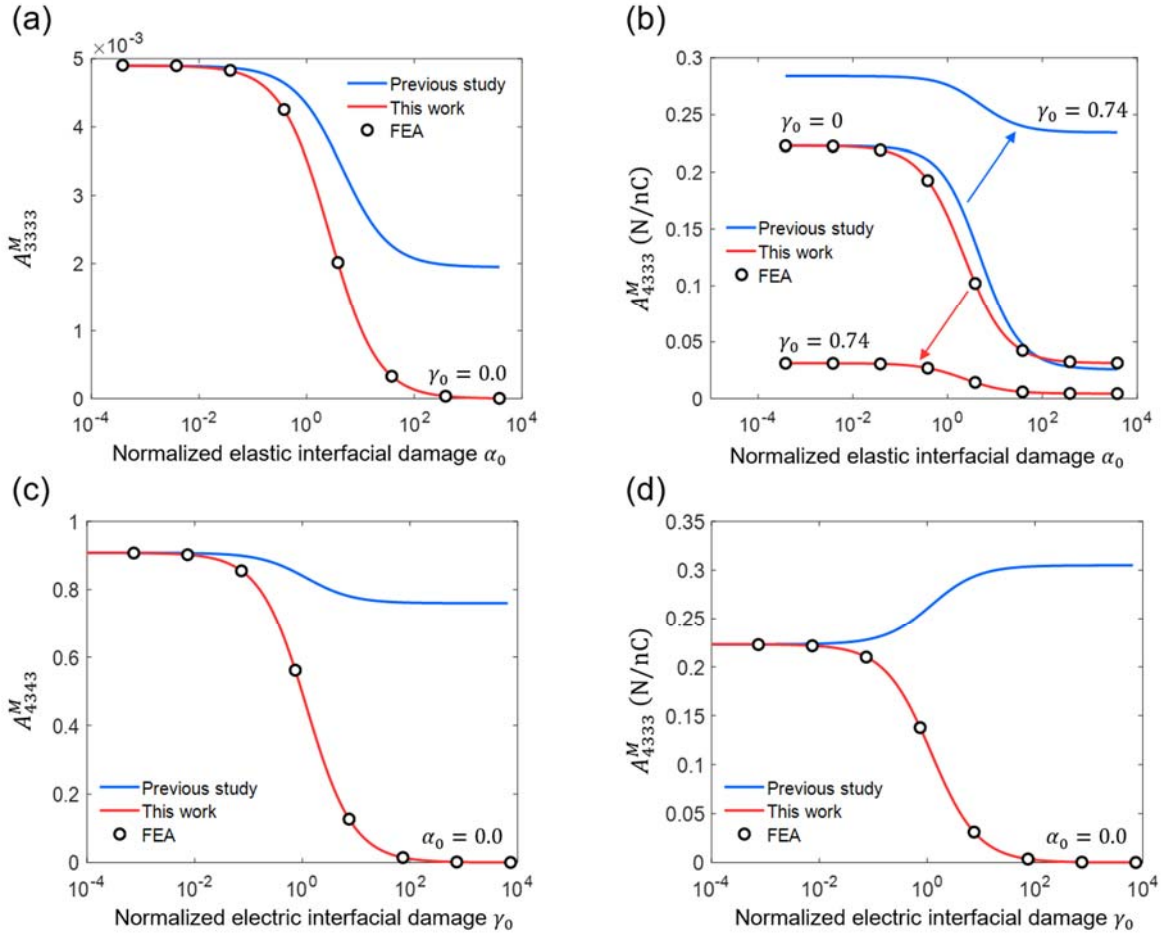

Fig. 6. (a) A^M_{3333}, (b) A^M_{4333}, and (c) A^M_{4343} as a function of the normalized elastic interfacial damage. (d) A^M_{4333} with respect to the normalized electric interfacial damage. We normalized the interfacial damage by $\alpha_0 = C^0_{1111}\alpha/a$, $\gamma_0 = \kappa^0_{11}\gamma/a$ where C^0_{1111} and κ^0_{11} are the elastic stiffness and dielectric constant of the matrix, respectively. We also present the results obtained from equations used in the previous study (Wang et al., 2014c).

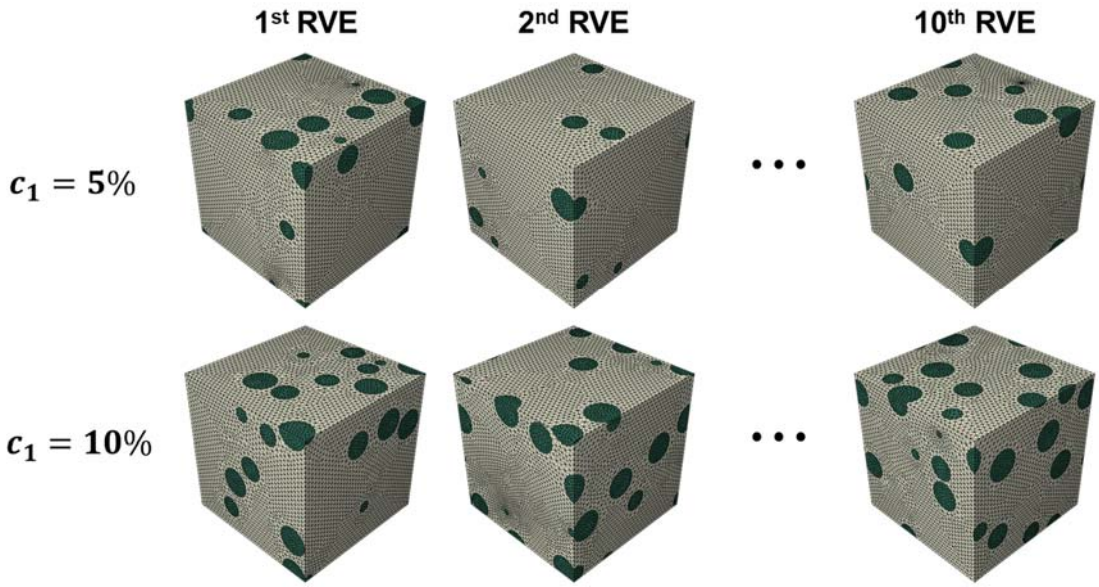

Fig. 7. Mesh configuration of the independent RVEs at two volume fractions.

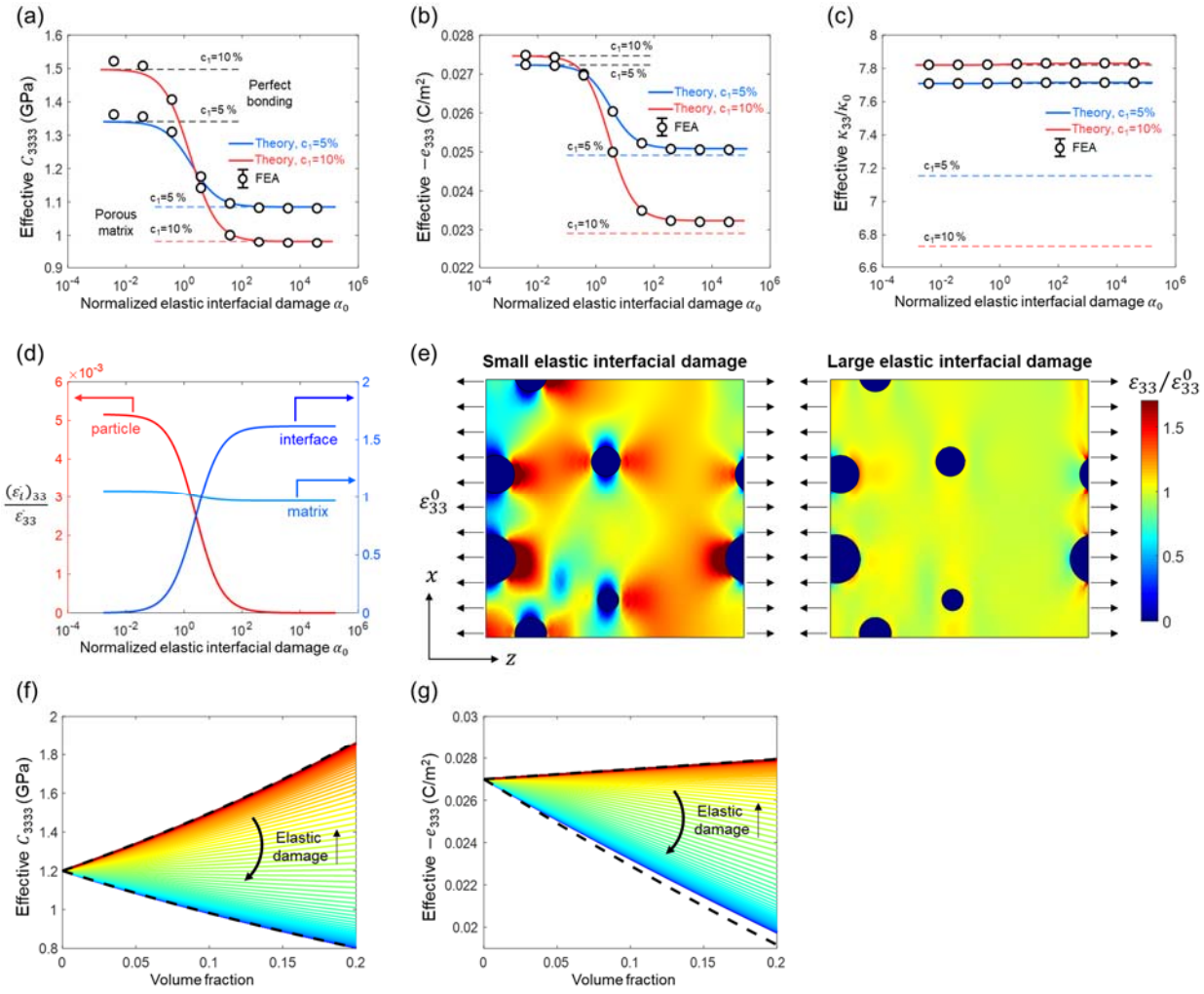

Fig. 8. (a) Effective elastic stiffness, (b) piezoelectric constant, and (c) dielectric constant of SiC–PVDF composite with respect to the normalized elastic interfacial damage. (d) Volume averaged strain$(\bar{\varepsilon}_i)_{33}$ within each phase under the applied strain $(\bar{\varepsilon}_{33})$. (e) FEA results of ε_{33} field under the applied ε^0_{33} for two interfacial damages (small elastic interfacial damage of 0.038, large elastic interfacial damage of 3.8). (f) Effective stiffness and (g) $-e_{333}$ with respect to the SiC particle volume fraction changing the elastic interfacial damage.

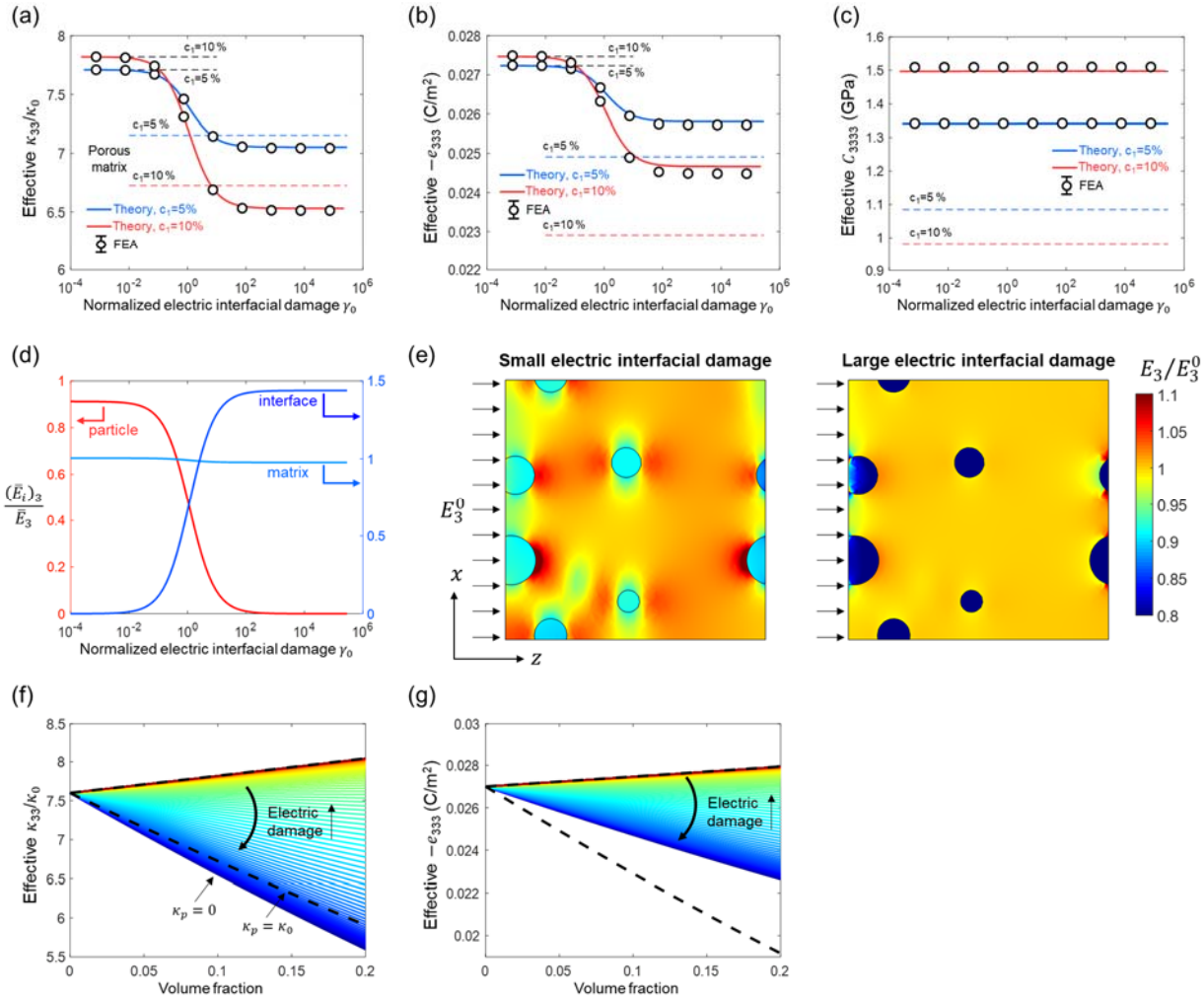

Fig. 9. (a) Effective dielectric constant, (b) piezoelectric constant, and (c) elastic stiffness of the SiC–PVDF composite with respect to the normalized electric interfacial damage. (d) Volume averaged electric field $(\bar{E}_i)_3$ within each phase under the applied electric field $(\bar{E}_3)$. (e) FEA results of the E_3 field under the applied E_3^0 for two interfacial damages (small electric interfacial damage of 0.0074, large electric interfacial damage of 0.2059). (f) Effective stiffness and (g) $-e_{333}$ with respect to the SiC particle volume fraction changing the electric interfacial damage. The upper and lower dashed lines represent the perfect bonding and porous results $(\kappa_p/\kappa_0 = 1)$, respectively.

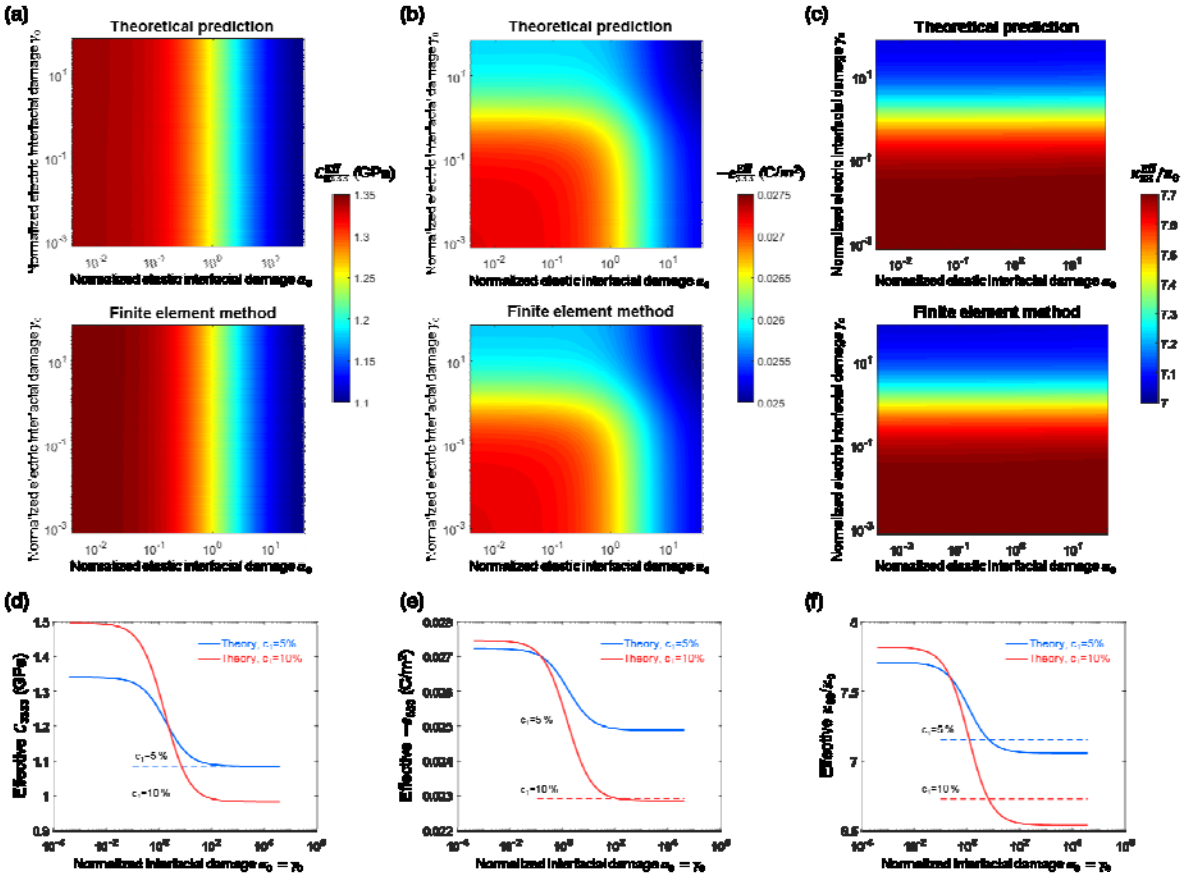

Fig. 10. (a) Effective stiffness, (b) piezoelectric constant, and (c) dielectric constant for two interfacial damages under fixed volume fraction of 5%. (d) Effective stiffness, (e) piezoelectric constant, and (f) dielectric constant when the two normalized interfacial damages are the same $(\alpha_0 = \gamma_0)$.

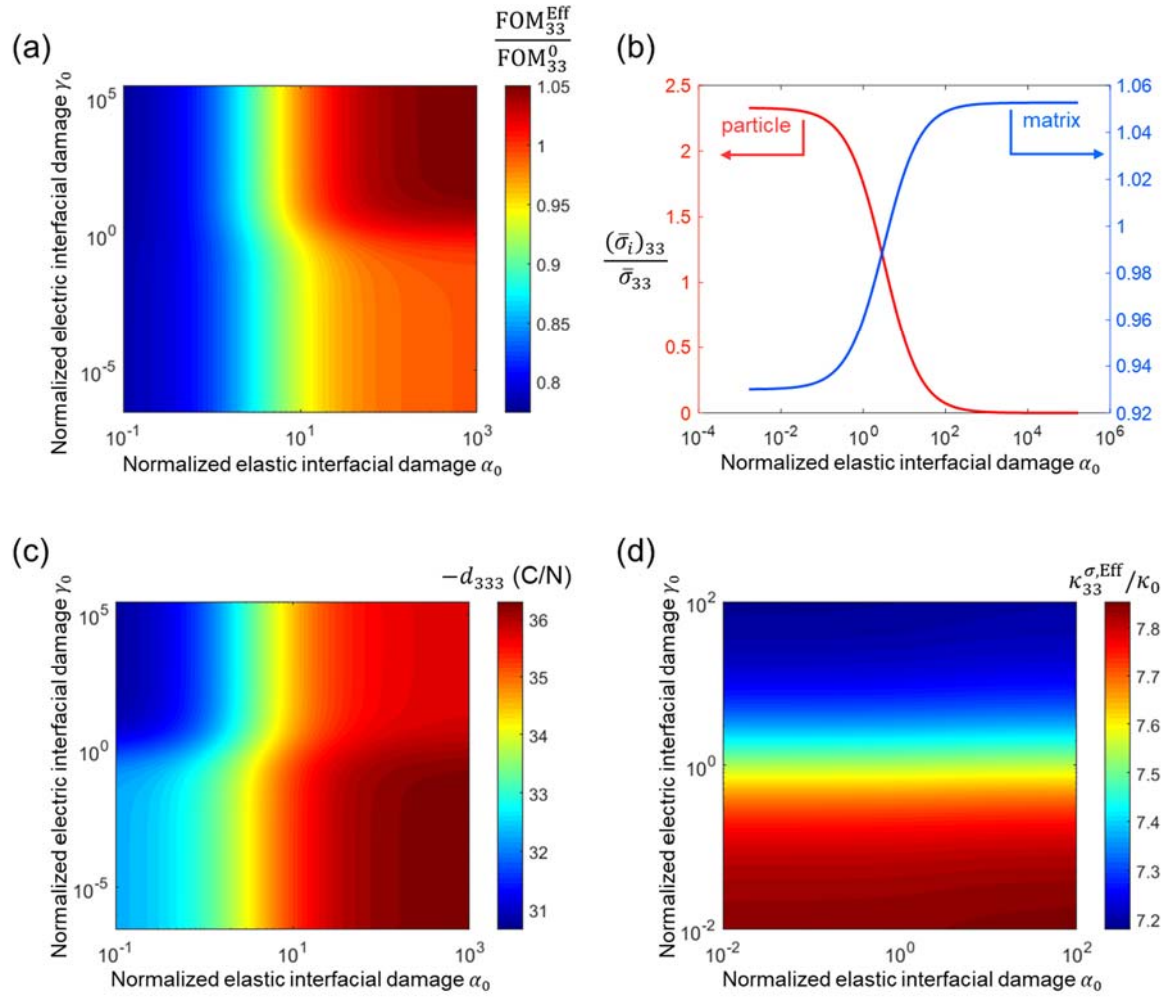

Fig. 11. (a) Normalized effective FOM_{33} of the composite, where the FOM_{33}^{0} is the FOM_{33} of the pure matrix (PVDF). (b) Volume averaged stress field within each phase under the applied stress. (c) Effective $-d_{333}$ and (d) $\kappa_{33}^{\sigma,\mathrm{Eff}}/\kappa_0$ for two interfacial damages. The volume fraction is 5%.

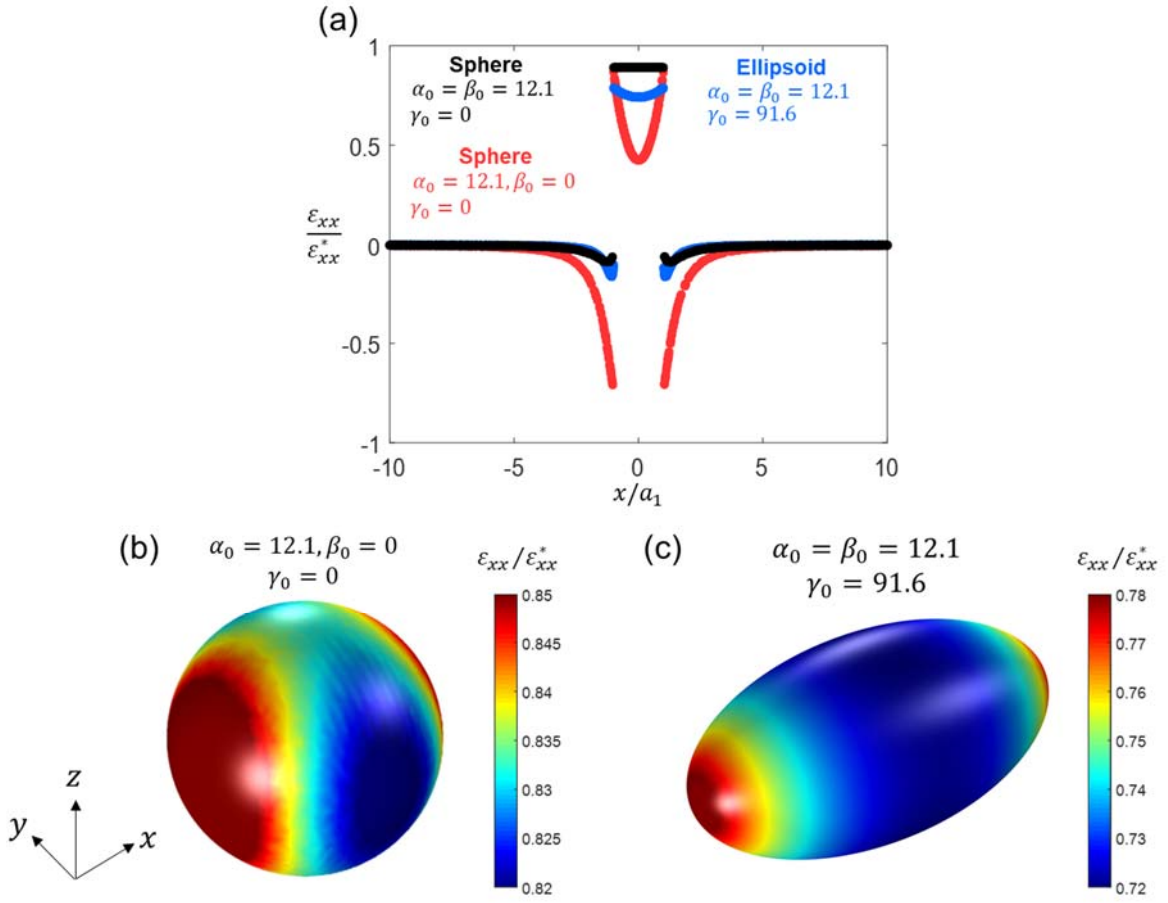

Fig. A1. (a) Strain field within the inclusion (PZT-5A) for different shape and interfacial damage parameters. Non-uniform strain field within (b) sphere and (c) spheroid with aspect ratio of 2. The minor axis is used for the normalized interfacial damage.

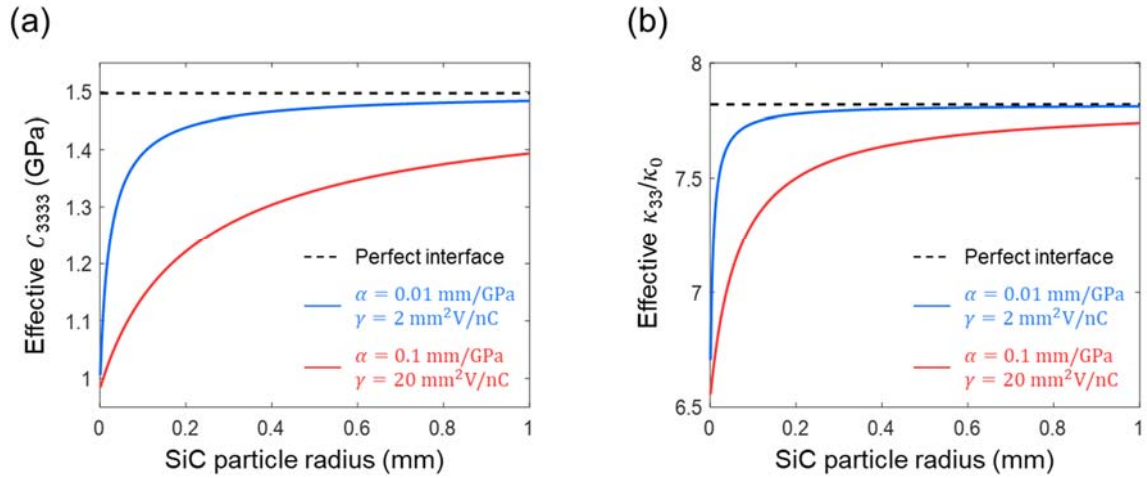

Fig. C1. Effective (a) elastic stiffness and (c) dielectric constant of the SiC–PVDF composite with respect to the size of the particle at fixed interfacial damages. The volume fraction of the particle is 5%.

References

Almusallam, A., Yang, K., Zhu, D., Torah, R.N., Komolafe, A., Tudor, J., Beeby, S.P., 2015. Clamping effect on the piezoelectric responses of screen-printed low temperature PZT/Polymer films on flexible substrates. Smart Mater Struct 24.

Barai, P., Weng, G.J., 2011. A theory of plasticity for carbon nanotube reinforced composites. Int J Plasticity 27, 539-559.

Barnett, D.M., Lothe, J., 1975. Dislocations and Line Charges in Anisotropic Piezoelectric Insulators. Phys Status Solidi B 67, 105-111.

Benveniste, Y., 1987. A New Approach to the Application of Mori-Tanaka Theory in Composite-Materials. Mech Mater 6, 147-157.

Bonfoh, N., Dreistadt, C., Sabar, H., 2017. Micromechanical modeling of the anisotropic thermal conductivity of ellipsoidal inclusion-reinforced composite materials with weakly conducting interfaces. Int J Heat Mass Tran 108, 1727-1739.

Bouhala, L., Makradi, A., Belouettar, S., Kiefer-Kamal, H., Freres, P., 2013. Modelling of failure in long fibres reinforced composites by X-FEM and cohesive zone model. Compos Part B-Eng 55, 352-361.

Cady, W.G., 1964. Piezoelectricity: an introduction to the theory and applications of electomechanical phenomena in crystals.

Chorsi, M.T., Curry, E.J., Chorsi, H.T., Das, R., Baroody, J., Purohit, P.K., Ilies, H., Nguyen, T.D., 2019. Piezoelectric Biomaterials for Sensors and Actuators. Adv Mater 31.

Comsol, 2015. v. 5.3. COMSOL AB, Stockholm, Sweden.

Dunn, M.L., Taya, M., 1993a. An Analysis of Piezoelectric Composite-Materials Containing Ellipsoidal Inhomogeneities. P Roy Soc Lond a Mat 443, 265-287.

Dunn, M.L., Taya, M., 1993b. Electromechanical Properties of Porous Piezoelectric Ceramics. J Am Ceram Soc 76, 1697-1706.

Dunn, M.L., Taya, M., 1993c. Micromechanics Predictions of the Effective Electroelastic Moduli of Piezoelectric Composites. Int J Solids Struct 30, 161-175.

Fan, J.D., Tadmor, E.B., 2019. Rescaling cohesive element properties for mesh independent fracture simulations. Eng Fract Mech 213, 89-99.

Folland, G.B., 2013. Real analysis: modern techniques and their applications. John Wiley & Sons.

Giordano, S., Palla, P.L., 2008. Dielectric behavior of anisotropic inhomogeneities: interior and exterior point Eshelby tensors. J Phys a-Math Theor 41.

Guerin, S., O'Donnell, J., Haq, E.U., McKeown, C., Silien, C., Rhen, F.M.F., Soulimane, T., Tofail, S.A.M., Thompson, D., 2019. Racemic Amino Acid Piezoelectric Transducer. Physical Review Letters 122, 047701.

Huang, J.H., Yu, J.S., 1994. Electroelastic Eshelby Tensors for an Ellipsoidal Piezoelectric Inclusion. Compos Eng 4, 1169-1182.

Jella, V., Ippili, S., Eom, J.H., Pammi, S.V.N., Jung, J.S., Tran, V.D., Nguyen, V.H., Kirakosyan, A., Yun, S., Kim, D., Sihn, M.R., Choi, J., Kim, Y.J., Kim, H.J., Yoon, S.G., 2019. A comprehensive review of flexible piezoelectric generators based on organic-inorganic metal halide perovskites. Nano Energy 57, 74-

93.
Jung, J., Lee, S., Ryu, B., Ryu, S., 2018. Investigation of effective thermoelectric properties of composite with interfacial resistance using micromechanics-based homogenisation. eprint arXiv:1811.11340, arXiv:1811.11340.
Kim, S.Y., Tanimoto, T., Uchino, K., Nam, C.H., Nam, S., Lee, W.I., 2011. Effects of PZT particle-enhanced ply interfaces on the vibration damping behavior of CFRP composites. Compos Part a-Appl S 42, 1477-1482.
Lee, K.Y., Kim, D., Lee, J.H., Kim, T.Y., Gupta, M.K., Kim, S.W., 2014. Unidirectional High-Power Generation via Stress-Induced Dipole Alignment from ZnSnO3 Nanocubes/Polymer Hybrid Piezoelectric Nanogenerator. Adv Funct Mater 24, 37-43.
Lee, S., Kim, Y., Lee, J., Ryu, S., 2019a. Applicability of the interface spring model for micromechanical analyses with interfacial imperfections to predict the modified exterior Eshelby tensor and effective modulus. Mathematics and Mechanics of Solids, 1081286519826343.
Lee, S., Lee, J., Ryu, B., Ryu, S., 2018. A micromechanics-based analytical solution for the effective thermal conductivity of composites with orthotropic matrices and interfacial thermal resistance. Scientific Reports 8, 7266.
Lee, S., Lee, J., Ryu, S., 2019b. Modified Eshelby tensor for an anisotropic matrix with interfacial damage. Mathematics and Mechanics of Solids 24, 1749-1762.
Lee, S., Ryu, S., 2018. Theoretical study of the effective modulus of a composite considering the orientation distribution of the fillers and the interfacial damage. Eur J Mech a-Solid 72, 79-87.
Li, J.P., Huang, H., Morita, T., 2019. Stepping piezoelectric actuators with large working stroke for nano-positioning systems: A review. Sensor Actuat a-Phys 292, 39-51.
Lin, J., Liu, W.Z., 2006. Experimental evaluation of a piezoelectric vibration absorber using a simplified fuzzy controller in a cantilever beam. J Sound Vib 296, 567-582.
Martinez-Ayuso, G., Friswell, M.I., Adhikari, S., Khodaparast, H.H., Berger, H., 2017. Homogenization of porous piezoelectric materials. Int J Solids Struct 113, 218-229.
Mikata, Y., 2001. Explicit determination of piezoelectric Eshelby tensors for a spheroidal inclusion. Int J Solids Struct 38, 7045-7063.
Mura, T., 1982. Micromechanics of defects in solids. Martinus Nijhoff Publishers.
Odegard, G.M., 2004. Constitutive modeling of piezoelectric polymer composites. Acta Mater 52, 5315-5330.
Othmani, Y., Delannay, L., Doghri, I., 2011. Equivalent inclusion solution adapted to particle debonding with a non-linear cohesive law. Int J Solids Struct 48, 3326-3335.
Pei, Y., Zeng, X.C., 2011. Elastic properties of poly(vinyldene fluoride) (PVDF) crystals: A density functional theory study. J Appl Phys 109.
Qu, J.M., 1993. The Effect of Slightly Weakened Interfaces on the Overall Elastic Properties of Composite-Materials. Mech Mater 14, 269-281.
Quang, H.L., He, Q.C., Bonnet, G., 2011. Eshelby's tensor fields and effective conductivity of composites made of anisotropic phases with Kapitza's interface thermal resistance. Philos Mag 91,

3358-3392.
Ramadan, K.S., Sameoto, D., Evoy, S., 2014. A review of piezoelectric polymers as functional materials for electromechanical transducers. Smart Mater Struct 23.
Ryu, S., Lee, S., Jung, J., Lee, J., Kim, Y., 2019. Micromechanics-Based Homogenization of the Effective Physical Properties of Composites With an Anisotropic Matrix and Interfacial Imperfections. Front Mater 6.
Springer, M., Turon, A., Pettermann, H.E., 2019. A thermo-mechanical cyclic cohesive zone model for variable amplitude loading and mixed-mode behavior. Int J Solids Struct 159, 257-271.
Stamatellou, A.M., Kalfas, A.I., 2018. Experimental investigation of energy harvesting from swirling flows using a piezoelectric film transducer. Energ Convers Manage 171, 1405-1415.
Tan, T., Yan, Z.M., Zou, Y.J., Zhang, W.M., 2019. Optimal dual-functional design for a piezoelectric autoparametric vibration absorber. Mech Syst Signal Pr 123, 513-532.
Venkatragavaraj, E., Satish, B., Vinod, P.R., Vijaya, M.S., 2001. Piezoelectric properties of ferroelectric PZT-polymer composites. J Phys D Appl Phys 34, 487-492.
Wang, S.P., Rong, W.B., Wang, L.F., Xie, H., Sun, L.N., Mills, J.K., 2019. A novel linear-rotary piezoelectric positioning stage based on surface's rectangular trajectory driving. Precis Eng 55, 376-380.
Wang, Z., Jin, X.Y., Chen, W.Q., Zhang, C., Fu, C.Q., Gong, H.Y., 2014a. Micro-scaled size-dependence of the effective properties of 0-3 PZT-cement composites: Experiments and modeling. Compos Sci Technol 105, 183-189.
Wang, Z., Zhu, J., Chen, W.Q., Jin, X.Y., Zhang, C.Z., 2014b. Modified Eshelby tensor for an ellipsoidal inclusion imperfectly embedded in an infinite piezoelectric medium. Mech Mater 74, 56-66.
Wang, Z., Zhu, J., Jin, X.Y., Chen, W.Q., Zhang, C., 2014c. Effective moduli of ellipsoidal particle reinforced piezoelectric composites with imperfect interfaces. J Mech Phys Solids 65, 138-156.
Yanase, K., Ju, J.W., 2012. Effective Elastic Moduli of Spherical Particle Reinforced Composites Containing Imperfect Interfaces. Int J Damage Mech 21, 97-127.
Yang, R.S., Qin, Y., Dai, L.M., Wang, Z.L., 2009. Power generation with laterally packaged piezoelectric fine wires. Nat Nanotechnol 4, 34-39.
Yuan, H., Lei, T.M., Qin, Y., Yang, R.S., 2019. Flexible electronic skins based on piezoelectric nanogenerators and piezotronics. Nano Energy 59, 84-90.
Zhang, Y., Xie, M.Y., Roscow, J., Bao, Y.X., Zhou, K.C., Zhang, D., Bowen, C.R., 2017. Enhanced pyroelectric and piezoelectric properties of PZT with aligned porosity for energy harvesting applications. J Mater Chem A 5, 6569-6580.
Zhang, Z.C., Gu, Y.Z., Wang, S.K., Li, M., Bi, J.Y., Zhang, Z.G., 2015. Enhancement of dielectric and electrical properties in BT/SiC/PVDF three-phase composite through microstructure tailoring. Compos Part a-Appl S 74, 88-95.
Zhao, J., Ho, K.K.C., Shamsuddin, S.R., Bismarck, A., Dutschk, V., 2012. A comparative study of fibre/matrix interface in glass fibre reinforced polyvinylidene fluoride composites. Colloid Surface

A 413, 58-64.
Zhong, Z., Meguid, S.A., 1997. On the elastic field of a spherical inhomogeneity with an imperfectly bonded interface. J Elasticity 46, 91-113.
Zhou, W.Y., Chen, Q.G., Sui, X.Z., Dong, L.N., Wang, Z.J., 2015. Enhanced thermal conductivity and dielectric properties of Al/beta-SiCw/PVDF composites. Compos Part a-Appl S 71, 184-191.